

DIGITAL HOLOGRAPHY AND HYBRID OPTO-ACOUSTIC IMAGING
SYSTEM FOR VIBRATION ANALYSIS

by

Muharrem Bayraktar

Submitted to the Graduate School of Engineering and Natural Sciences
in partial fulfillment of
the requirements for the degree of
Master of Science

Sabancı University

January 2010

DIGITAL HOLOGRAPHY AND HYBRID OPTO-ACOUSTIC IMAGING
SYSTEM FOR VIBRATION ANALYSIS

APPROVED BY:

Assoc. Prof. Dr. Meriç Özcan, (Dissertation Supervisor)

.....

Assist. Prof. Dr. Ayhan Bozkurt

.....

Assist. Prof. Dr. Gözde Ünal

.....

Assist. Prof. Dr. Güllü Kızıldağ Şendur

.....

Assoc. Prof. Dr. İbrahim Tekin

.....

DATE OF APPROVAL:

© Muharrem Bayraktar 2010

All Rights Reserved

To my family

Acknowledgements

First of all, I would like to express my utmost appreciation to my thesis supervisor Assoc. Prof. Dr. Meriç Özcan for guiding me during the thesis research. Thank him for his support, advice and encouragement both as a mentor and an academician. Moreover, I want to thank all of my professors for their teaching during my undergraduate and graduate study. I also thank to my thesis defense committee members Ayhan Bozkurt, Gözde Ünal, Güllü Kızıldaş Şendur and İbrahim Tekin for their constructive comments and presences.

TÜBİTAK and Sabancı University funded this thesis research and also they supported me with their scholarship. I want to thank these institutions for enabling my education.

Furthermore, I would like to express my special thanks to my friends. I shared most of my time with you; we enjoyed much and you kept my energy high.

Last but not least, I would like to thank all with my heart to my beloved family for their endless support to pursue my ambitions. You were physically far, but sensationally always with me since early times of my education.

DIGITAL HOLOGRAPHY AND HYBRID OPTO-ACOUSTIC IMAGING SYSTEM FOR VIBRATION ANALYSIS

MUHARREM BAYRAKTAR

EE, M.Sc. Thesis, 2010

Thesis Supervisor: Assoc. Prof. Dr. Meriç Özcan

Keywords: holography, digital holography, diffraction calculation, computer generated holography, referenceless holography, interferometry, microphone arrays, vibration analysis

Abstract

Holography is a true three dimensional (3D) imaging technique that has real life applications varying from high resolution 3D microscopy to interferometric analysis. In this thesis a hybrid opto-acoustic vibration analysis system is designed and implemented which is combination of a digital holographic interferometer and an acoustic microphone array. The system is capable of analyzing broad range of vibration amplitudes by utilizing acoustic microphone array for coarser analysis and holographic interferometer for small scale analysis on the order of few hundred nanometers. In the design process of the system, a comprehensive research on holography is performed both from theoretical and practical perspectives. In the theoretical part, a discrepancy that exists in the literature for the numerical reconstruction of digital holograms is clarified and a new method for diffraction pattern calculation is presented which we call Planar Layers Method (PLM). PLM is a fast method based on the idea of representing 3D computer synthesized objects with discrete planar layers and evaluating the diffraction patterns efficiently using Fast Fourier Transform (FFT) based Fresnel Transform. In the practical issues about holography, a new holographic recording scheme is presented in which there is no need for a separate reference wave. In the method reference beam is generated from the reflecting object wave, therefore path length equalization can be done automatically.

DİJİTAL HOLOGRAFI VE HİBRİT OPTO-AKUSTİK GÖRÜNTÜLEME SİSTEMİYLE TİTREŞİM ANALİZİ

MUHARREM BAYRAKTAR

EE, Yüksek Lisans Tezi, 2010

Tez Danışmanı: Doç. Dr. Meriç Özcan

Anahtar Kelimeler: holografi, dijital holografi, dağılma hesaplaması, bilgisayarda üretilmiş holografi, referanssız holografi, interferometre, mikrofondizileri, titreşim analizi

Özet

Holografi, yüksek çözünürlüklü üç boyutlu (3B) mikroskopik görüntülemeinden interferometrik denetime kadar çeşitli uygulamaları olan bir gerçek 3B görüntüleme yöntemidir. Bu tezde bir dijital holografik interferometrenin ve bir akustik mikrofondizisinin birleşimi olan hibrit opto-akustik titreşim analizi sistemi tasarlanmış ve sistem kullanılarak çeşitli nesnelere analiz edilmiştir. Sistem geniş bir titreşim büyüklüğü aralığını akustik mikrofondizisini kullanarak geniş ölçekte, holografik interferometreyi kullanarak da birkaç yüz nanometreye kadar küçük ölçekte analiz edebilmektedir. Sistemin tasarım sürecinde, holografi üzerine teorik ve pratik açıdan kapsamlı bir akademik araştırma yürütülmüştür. Teorik kısımda, dijital hologramların sayısal olarak yeniden yapılandırılmasında genellikle karşılaşılan bir karışıklık açığa kavuşturulmuştur ve dağılma desenlerinin hesaplanmasında yeni bir yöntem olan Düzlemsel Katmanlar Yöntemi (DKY) sunulmuştur. DKY, bilgisayarda sentezlenmiş 3B nesnelere düzlemsel katmanlara ayrılmasını ve bu katmanların dağılma desenlerinin hızlı Fourier dönüşümü (HFD) temelli Fresnel dönüşümü kullanılarak hesaplanması fikri üzerine kurulmuş hızlı bir yöntemdir. Holografi ile ilgili pratik konularda ise ayrı bir referans dalgasına ihtiyaç duymayan yeni bir holografik kayıt düzeni sunulmuştur. Bu yöntemde referans dalgası yansıyan nesne dalgasından üretilmiştir, bu yüzden dalgaların katettiği mesafeler otomatik olarak eşitlenmiştir.

TABLE OF CONTENTS

Acknowledgements	iii
Abstract	iv
Özet	v
List of Figures	viii
1 INTRODUCTION	1
1.1 Holography	6
1.1.1 Filtering With Multiple Captures	10
1.1.2 Spatial Filtering	13
1.1.3 Other Filtering Techniques	16
2 DIGITAL HOLOGRAPHY RECONSTRUCTION METHODS	17
2.1 Diffraction Calculation	17
2.1.1 Fresnel Transform	18
2.1.2 Convolution Method	22
2.2 Numerical Results	25
3 A METHOD FOR COMPUTER GENERATED HOLOGRAPHY	31
3.1 Planar Layers Method (PLM)	34
3.2 Numerical Results	36
4 HOLOGRAPHIC RECORDING WITHOUT A SEPARATE REFERENCE WAVE	39
4.1 Experimental Setup	40
4.2 Results	42

5	HOLOGRAPHIC INTERFEROMETER AND MICROPHONE ARRAY SYSTEM FOR IMAGING AND ANALYSIS OF VI- BRATING SURFACES	45
5.1	Holographic Deflection Measurement	46
5.1.1	Simulation Results	47
5.1.2	Experimental Results	49
5.2	Holographic Vibration Analysis	50
5.2.1	Simulation Results	52
5.2.2	Experimental Results	54
5.3	Acoustic Vibration Analysis	55
5.3.1	Car Door Experiment	56
5.3.2	Aluminum Plate Experiment	57
5.4	Experiments with the Hybrid Opto-Acoustic Imaging System	61
5.4.1	Car Door Experiment	61
5.4.2	Aluminum Plate Experiment	64
6	CONCLUSIONS AND FUTURE PROSPECTS	67
6.1	Conclusion	67
6.2	Future Prospects	68

List of Figures

1.1	A typical holographic recording scheme	6
1.2	Holographic reconstruction scheme	8
1.3	(a) Object to be recorded holographically. It is padded with zeros in order to avoid aliasing. (b) Reconstructed off-axis hologram without any filtering. Because of off-axis recording geometry images are not co-centric, i.e. zero-order image is at the center, focused virtual image is at the lower right and defocused real image is at the upper left. Zero-order and the real image partially blocks the virtual image. . . .	9
1.4	Zero-order image is filtered using two phase shifted holograms. Most part of the virtual image is clear but defocused real image again partially blocks the virtual image.	11
1.5	Zero-order and the conjugate images are filtered using phase shifted holograms.	12
1.6	In this figure an experimentally recorded hologram of a dice is seen. Left column consists of unfiltered holograms and right column consists of filtered holograms. (a) Recorded off-axis hologram and filtered hologram. (b) Frequency spectrum of the holograms. (c) Reconstruction results.	14
2.1	Left: Coordinate system used in derivation of Fresnel diffraction equation, both planes are centered around zero. Right: As it is explained in the text if bounds of the summations are set to start from zero without properly shifting the indices, the diffraction integral is calculated in this coordinate system.	18

- 2.2 (a) 1534×1024 pixels hologram of a dice recorded in off-line configuration with a 30 mW HeNe laser. The pixel dimensions are $9 \mu m \times 9 \mu m$ and the object distance d is 89 cm. (b) Amplitude and phase of the reconstructed hologram that is computed using Eq. 2.9. The image of the object is not at the right place. (c) Amplitude and phase of the reconstructed hologram by Method 1, using Eq. 2.14 and finally, (d) Amplitude and phase of the reconstructed hologram by Method 2, using Eq. 2.15. Last two methods produce exactly the same results as expected. Note that the actual pixel dimensions in the reconstructed image is different (ratio of vertical-pixel size to horizontal-pixel size is $1534/1024$) as given by Eq. 2.5 which means that the physical size of the reconstructed holograms is same in both vertical and horizontal directions. Here we show the pixel values so the reconstructed holograms look like the same size as the hologram. 26
- 2.3 An example of computer generated holography. From the 512×512 planar object shown (Yumoş, the cat with a hat) in (a) off-axis holograms were calculated using Fresnel diffraction equation at three different distances with a reference wave that has 0.3° angle with both transverse axes. The pixel dimension of the image is taken as $40 \mu m \times 40 \mu m$. Then using phase shift holography method to remove the zero order term object is reconstructed where (b), (c), and (d) shows the magnitude of reconstructed holograms. Left column is calculated by using the correct version of the diffraction equation (Eq. 2.15) and the right column is calculated using Eq. 2.9. As the distance decreases the effect of the quadrature terms become more significant and it is the reason for the distortion seen in the bottom row images. 28
- 2.4 (a) A (256 by 256) input image, pixel dimensions are assumed to be $30 \mu m \times 30 \mu m$. (b) Far field magnitude and phase plots for $d = 1 m$ calculated by the correct discrete Fresnel equation, pixel size $82 \mu m \times 82 \mu m$, (c) Far field magnitude and phase plots for $d = 1 m$ calculated by the convolution approach (Eq. 2.19). In convolution calculation zeroes are padded around the image to prevent the aliasing as it is explained in the text, here we show the central 256×256 pixels of the resulting image. We see $\approx 82/30$ times magnified portion of the far field distribution with the convolution approach as expected. For this example with a 1.75 GHz Pentium PC, discrete Fresnel approximation calculation by FFT takes ≈ 0.22 sec, convolution via FFT takes ≈ 1.48 sec and direct convolution is ≈ 30 sec (not shown) using Matlab software. 29

2.5	(a) A (512 by 512) input image, pixel dimensions are assumed to be $30\mu m \times 30\mu m$. (b) Far field magnitude and phase plots for $d = 1 m$ calculated by the correct discrete Fresnel equation, pixel size $41\mu m \times 41\mu m$, (c) Far field magnitude and phase plots for $d = 1 m$ calculated by the convolution approach (Eq. 2.19). In convolution calculation zeroes are padded around the image to prevent the aliasing as it is explained in the text, here we show that the central 512×512 pixels of the resulting image. We see $\approx 41/30$ times magnified portion of the far field distribution with the convolution approach as expected. For this example with a 1.75 GHz Pentium PC, discrete Fresnel approximation calculation by FFT takes ≈ 0.89 sec, convolution via FFT takes ≈ 11 sec and direct convolution is ≈ 480 sec (not shown) using Matlab software.	30
3.1	Perspective view of a simple pyramid. For this pyramid intensity map and depth map that is seen from z-axis is shown. In order to propagate using PLM, for each depth value ($z = 0.70, 0.71, 0.72, 0.73$) corresponding intensity values are taken from intensity map and the remaining parts are padded with zeros.	35
3.2	(a) A cube that is covered with USAF resolution chart with dimensions of $5.9 mm \times 5.9 mm \times 5.9 mm$. It is rotated by 45° in x and y axes. (b) Depth map for the cube. There are 202 unique depth values where nearest point is at $d = 0.7 m$ and farthest point is at $d = 0.7071 m$. (c) Object wave of the cube calculated using PPM. (d) Object wave that is calculated using PLM. Visually they are quite same but a more proper error analysis is done in the text.	37
3.3	Reconstruction results at $d=0.7$ meter for the holograms generated by (a) PPM and (b) PLM	38

- 4.1 Setup for recording holograms without a separate reference wave. Lens 1 and Lens 2 and a pinhole (PH) is used for cleaning up and enlarging the laser beam. The object wave is split with a beamsplitter (BS1) and one of the beams is focused into a single mode fiber with a lens (L3). At the exit end of the fiber is the reference wave and it is converted to a plane wave with another lens (L4). The resultant reference wave is combined over a second beamsplitter (BS2)-rotated slightly for off-axis hologram recording- with the other part of the object beam routed around with two mirrors (M1 and M2). Two combined waves are allowed to interfere at the CCD and the interference intensity is recorded. Note that there is a variable attenuator (VA) in the path of the object beam after the first beam splitter in order to equalize powers in the reference wave and the object wave to maximize the interference pattern as it is explained in the text. 41
- 4.2 a) 1534×1024 pixels hologram of the two coins recorded in off-axis configuration with a 30 mW HeNe laser. The pixel dimensions of the CCD are $9 \mu m \times 9 \mu m$. b) Magnitude of the reconstructed hologram at a distance of $d = 140 \text{ cm}$. It is clearly seen that the hologram of two coins are reconstructed successfully, zero order and the conjugate image is also apparent. Note that the reconstructed image is also 1534×1024 pixels but the pixel dimensions are different so that its actual shape becomes a square. Since from the Fresnel diffraction theory the pixel dimensions in the reconstructed image is: $\lambda d/N_x \Delta_x = 45.8 \mu m$ and $\lambda d/N_y \Delta_y = 68.6 \mu m$ for the horizontal and vertical directions where $N_x = 1534$ and $N_y = 1024$ are the number of pixels in the horizontal and vertical directions, $\Delta_x = \Delta_y = 9 \mu m$ and d is the object to CCD distance. 43
- 4.3 a) 1534×1024 pixels hologram of the two coins recorded in off-axis configuration with a 30 mW HeNe laser. The pixel dimensions of the CCD are $9 \mu m \times 9 \mu m$. b) Magnitude of the reconstructed hologram at a distance of $d = 140 \text{ cm}$. It is clearly seen that the hologram of two coins are reconstructed successfully, zero order and the conjugate image is also apparent. Note that the reconstructed image is also 1534×1024 pixels but the pixel dimensions are different so that its actual shape becomes a square. Since from the Fresnel diffraction theory the pixel dimensions in the reconstructed image is: $\lambda d/N_x \Delta_x = 45.8 \mu m$ and $\lambda d/N_y \Delta_y = 68.6 \mu m$ for the horizontal and vertical directions where $N_x = 1534$ and $N_y = 1024$ are the number of pixels in the horizontal and vertical directions, $\Delta_x = \Delta_y = 9 \mu m$ and d is the object to CCD distance. 44

5.1	(a) A circular surface is deflected from its center to the direction θ_e and observed from direction θ_o . (b) Deflection magnitude of $\Delta d = \lambda/2$ is represented by 128 layer. In the figure only 8 layers are shown. (c) Layer by layer representation of the surface is shown with the intensity profiles of three layers. First layer has a circular intensity profile and rest of the layers have gradually increasing ring shaped intensity profiles. (d) There is one dark-bright-dark transition as explained in the text since the deflection magnitude is $\Delta d = \lambda/2$. A cut from the center is also shown and there are distortions on the left part due to real image term.	48
5.2	(a) Holographic deflection recording scheme, (c) Photograph of the experimental setup (He-Ne: Laser, M: Mirror, BS: Beam splitter, CCD: CCD Camera).	49
5.3	(a) Experimental result and (b) simulation result for deflection magnitude of $3\mu m \approx 5\lambda$; there are 10 fringes from perimeter to center. (c) Experimental result and (d) simulation result for deflection magnitude $5\mu m \approx 8\lambda$; there are 16 fringes from perimeter to center.	51
5.4	Holograms of the vibrating surfaces are recorded with PLM method for resonant mode (a) u_{12} and (b) u_{21} . Nodal lines are bright and as vibration amplitude increases fringing occur due to the behavior of the Bessel function.	53
5.5	The loudspeaker (the same loudspeaker setup as in the deflection measurements) has resistance of 4Ω and it is driven over a series 47Ω resistor with a sine wave of amplitude 100 mV at two different resonant frequencies (a) 647 Hz and (b) 1290 Hz . Since the surface over the loudspeaker is not exactly rotationally or radially symmetric resulting fringes are not radially or rotationally symmetric.	54
5.6	(a) Head Acoustics MV210 microphone (b) Recording and amplification module Squadriga (c) A typical linear microphone array for noise recording.	57
5.7	(a) A car door and pressure maps over a $(22.4\text{ cm} \times 19.2\text{ cm})$ area while its window motor is working at different driving voltages. (b) 10 V , (c) 15 V and (d) 20 V . As the driving voltage increases pressure amplitude increases.	58
5.8	(a) Power amplifier. (b) Aluminum plate and the electromagnet setup.	59

5.9	(a) Aluminum plate and pressure maps of it over a ($22.4\text{ cm} \times 19.2\text{ cm}$) area when the electromagnet is driven by (b) 15 V and (c) 30 V	60
5.10	Hybrid opto-acoustic analysis system that is a combination of a holographic interferometer and a microphone array system.	62
5.11	Vibration characteristic of the car door motor at three different driving voltages. The area imaged by the holographic system is ($6.33\text{ cm} \times 6.33\text{ cm}$) as explained in the text. Fringe spacing becomes narrower as the driving voltage is increased (a) 10 V , (b) 15 V and (c) 20 V . The fringes are especially focused at the left side.	63
5.12	The same car door analyzed using the acoustics system when its window motor is driven by 20 V . The imaged area is ($11.2\text{ cm} \times 9.6\text{ cm}$). As in the holographic analysis vibration is mainly concentrated on the left side.	64
5.13	Vibration characteristic of a 2 mm thick aluminum plate. The imaged area is ($3.87\text{ cm} \times 3.87\text{ cm}$) as explained in the text. There are slanted vertical fringes and again the pattern becomes steeper as the voltage is increased from (b) 15 V to (c) 30 V	65
5.14	Analysis of the aluminum plate using the acoustic system. The imaged area is ($11.2\text{ cm} \times 9.6\text{ cm}$).	66

1 INTRODUCTION

Imaging can be defined as recording and representation of object's appearance in relation with visual sense. Imaging starts with first wall paintings of the human-being and it spans micro to macro scale objects, events and scenes. Today, it can be categorized as medical imaging, acoustic imaging, radar imaging, optical imaging and some other. In optical imaging, although high resolution two dimensional (2D) imaging is rather successful, it is always important to have three dimensional (3D) imaging in real life applications. 3D imaging techniques can be listed as stereoscopic or multiview imaging, integral imaging and holographic imaging. Stereoscopic imaging systems actually do not record real 3D information but they capture two images of a scene with a proper viewing angle difference. At the display side, two images are directed to both eyes with special viewing aids (such as eye glasses) and their combination in the brain creates the 3D feeling. Recent systems are autostereoscopic and it is not needed to use viewing tools to send different 2D views of the scene [1]. Integral imaging and holography are also inherently autostereoscopic techniques. In integral imaging, different depths of objects are picked up with a lens array [2]. Recorded information is revealed by back tracing the recording beams. Advances in microfabrication technology made possible to fabricate smaller microlens arrays. This progress increased the resolution hence the integral imaging became popular again. Among these techniques holography is the only true 3D imaging technique [3]. In holography it is possible to recreate an exact replica of the recorded object wave field including all of the 3D properties such as shape, texture, color and most importantly all of the depth cues.

In 2D imaging, specifically in photography, intensity of an object wave that reaches to a recording medium or a device is captured. Intensity pattern is dependent only on magnitude of the incoming object wave but the phase information which encodes the sense of depth is lost in the process. On the other hand in the holography process, object wave and a coherent reference wave is interfered and resulting interference pattern is recorded. Although the recorded information is a 2D intensity pattern it is possible to retrieve the captured 3D information after reconstruction. Since the object wave information is captured and displayed completely holograms carry all of the depth cues. Important depth cues are occlusion, perspective, motion parallax, accommodation and binocular (retinal) disparity. Most dominant depth cue which is also present in 2D imaging is the occlusion which is the blockage of light coming from overlapping parts of objects. Perspective is the convergence of parallel lines such as light rays at the infinity which enables an observer to distinguish relative distances and sizes. Motion parallax is the relative view change of objects with respect to background as the observer moves. Accommodation is the oculomotor depth cue that is interpreted in the brain which is a result of stretching and squeezing of the eye lens with eye muscles to focus an object. Binocular or retinal disparity is the cue which depends on the slight angle difference between two views of an object between two retinas. This is also called stereopsis and it is the cue used in stereoscopic systems to create 3D feeling [4].

Holography was invented by Dennis Gabor in 1948 while he was working on improvement of resolution of an electron microscope. Hence holography is proposed as a new high resolution microscopy principle [3]. The word hologram is introduced by Gabor that inspired from the words "holo" meaning whole and "gram" meaning

writing/drawing in Greek. Holography is an interferometric technique which needs two coherent light sources at recording and reconstruction for better performance. Hence first holograms had problems since they are recorded using partially coherent light sources. This is a restriction that limited the progress of holography at early stages. After ten years, with the invention of coherent light source - the laser - in 1959, holography became a popular research area [5]. In 1962, off-axis holography is invented which underlined imaging feature of holography not only for microscopy applications but also for imaging in larger dimensions [6]. In the same year thick holograms were introduced which can be reconstructed using white light [7]. Within few years interferometric feature of holography started to have usage in testing applications such as surface contouring, deflection measurement and vibration analysis [8–10]. A different approach - computer generated holograms (CGH) - are first presented in 1969 by B. R. Brown and A. W. Lohman [11]. In 1970's with the development in digital electronics, idea of digital holography is born in which processing - especially reconstruction - of holograms on computers without any need for reconstruction illumination made the holography process more practical [12, 13]. With these advancements, a holographic video display system is demonstrated for the first time at MIT [14, 15]. Though the system reduces information content, it was working in real time. Up to now, a brief historical review on some aspects of holography is given that are closely related to this thesis. Besides those areas, holography is used in 3D imaging [16, 17], microscopy [3, 18, 19], imaging through turbid media [20–22], refractive index measurement [23], holographic data storage [20, 24, 25], object recognition [26–28], finding 3D locations of particles [29], watermarking [30] and 3D TV research [31]. These areas are not explored here but they may have a connection with the future directions of the thesis.

Despite such advantages of holography, there are some difficulties in the process. Some of these difficulties are lifted up within years:

1) For example requirement of coherent single wavelength light - probably the major problem -with the invention of laser. However lasers introduced a new problem called speckle noise that comes from unwanted and arbitrary interference of waves from different points of the objects [32].

2) Another difficulty was the recording material. When holograms are recorded on photographic films, development of them and reconstruction with real laser illumination limits the usage. Advances in digital electronics made possible to record holograms directly on CCD cameras and reconstruct them computationally on a computer. [33]. However low resolution of CCD cameras (200 lines/mm) compared to photographic films (up to 8000 lines/mm) became a challenge.

3) An important practical difficulty in recording is the mechanical stability of the setup. For example, instability on the order of quarter-wavelength of the light used in the recording may cause to wash out necessary interference fringes.

4) Beyond mechanical stability coherence of the object wave and the reference wave is another difficulty. In order to have a good interference path length difference between two interfering waves must be within the coherence length of the laser.

5) A different practical difficulty in holography lies in the reconstructed image of holograms especially in inline holograms. Reconstructed images of holograms contain exact replica of the object wave but they also contain inherent artifacts (zero-order and conjugate images) that are coupled to the object wave due to interference.

Although holography theoretically stands in a mature frame, all of these challenges are fertile areas for new ideas that attract scientists and researchers. With this vision our research aims to address some of the challenges in both 3D imaging and interferometric nature of holography.

The thesis is organized as follows: Rest of this chapter is devoted to explanation of mathematical and optical model for the holography and to explain the common terminology. In this chapter also two relatively intuitive filtering techniques to address the removal of artifacts (zero-order and conjugate images) in a reconstructed hologram is explained and references to other filtering techniques are given. In chapter 2 reconstruction methods that are used in digital holography is given and a discrepancy that is generally encountered in the literature is made clear [34]. In chapter 3 a new method what we call Planar Layers Method (PLM) for calculation of diffraction patterns in CGH is proposed with relevant literature survey [35]. After these theoretical issues a more practical idea to overcome the coherence length restriction of lasers is introduced in chapter 4 [36]. The presented idea makes possible to record holograms with low coherence length lasers hence reducing the setup cost. Chapter 5 starts with mathematical definition of the deflection measurement using holographic interferometry. Then, vibration analysis with holographic interferometry and microphone arrays is explained. In these sections mathematical descriptions are wrapped up with literature reviews. The methods are demonstrated with simulations using PLM and also experimental results are given. After these sections, a new hybrid testing system which is combination of a holographic interferometer and an acoustic microphone array is presented. To our knowledge this hybrid system is designed and implemented for the first time within this thesis. Capabilities of the hybrid system are demonstrated by comparative experiments. Conclusions and future directions provided by the thesis is summed up in chapter 6.

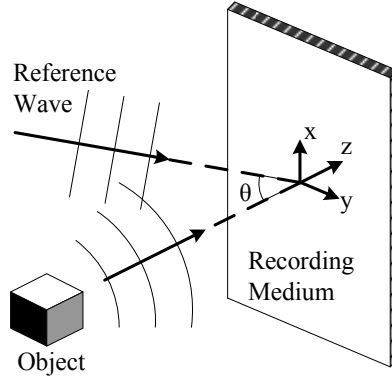


Figure 1.1: A typical holographic recording scheme

1.1 Holography

Holography strictly relies on interference of two coherent lights in the recording. To do so a laser beam is split into two arms, one is used to directly illuminate the recording medium which is referred as the reference wave U_r and the other one is used to illuminate the object. The wave diffracted from the object is called the object wave U_o and interference of the object wave and the reference wave is recorded as a hologram. A general recording scheme for transmission type off-axis holography [6] is shown in Fig. 1.1. For interference of two beams they must be coherent. First thing that comes into mind concerning coherence is the distances traveled by two waves. The difference of distance traveled by two arms must be within the coherence length of the laser. Polarization equality of two beams and mechanical stability are other two necessities for maximum interference. With this properties satisfied a reference beam is generally taken as a plane wave represented by:

$$U_r(x, y) = |U_r| \exp\{jkx \sin \theta\} \exp\{-jkz \cos \theta\}, \quad (1.1)$$

where k is the wave number and θ is the angle that U_r makes with the z -axis in the x - z plane as it is shown in Fig. 1.1. Then wave field created by the interference of U_o

and U_r will be:

$$U_h(x, y) = U_o(x, y) + U_r(x, y). \quad (1.2)$$

The captured pattern on the hologram will be intensity of this field represented by:

$$\begin{aligned} I_h(x, y) &= [U_o(x, y) + U_r(x, y)] [U_o(x, y) + U_r(x, y)]^* = |U_o + U_r|^2 \\ &= |U_o|^2 + |U_r|^2 + U_o U_r^* + U_o^* U_r, \end{aligned} \quad (1.3)$$

where $*$ is the complex conjugate operator. The term $|U_o|^2$ is called the self interference and distorts other terms since it is spatially varying. The second term $|U_r|^2$ is called the reference bias which is spatially invariant and corresponds to an increase in the intensity of the hologram; it is analogous to DC term in the signals. The cross-interference signal $U_o U_r^*$ is the exact replica of the object wave multiplied with a spatially invariant reference wave and $U_o^* U_r$ is the conjugate of the object wave multiplied with the reference wave. These two terms carry all the necessary 3D information if they can be extracted properly.

The extraction process which is shown in Fig. 1.2 is called the hologram reconstruction and it is done by illuminating the hologram with the reference wave.

$$\begin{aligned} U_c(x, y) &= U_r(x, y) I_h(x, y) \\ &= |U_o|^2 U_r + U_r |U_r|^2 + |U_r|^2 U_o + U_o^* U_r^2. \end{aligned} \quad (1.4)$$

As it is seen from the equation, third term is an exact replica of the object wave just multiplied with a constant term. Hence when the reconstructed hologram is viewed from the illumination direction, it appears like the wave is diffracting from hologram aperture to the original location of the object and forms a virtual duplicate of it. Hence third term is called the virtual image of the object. First term diffracts straightly in the reconstruction illumination direction with uniform wavefront amplitude since reference wave is a plane wave. Second term also diffracts along the

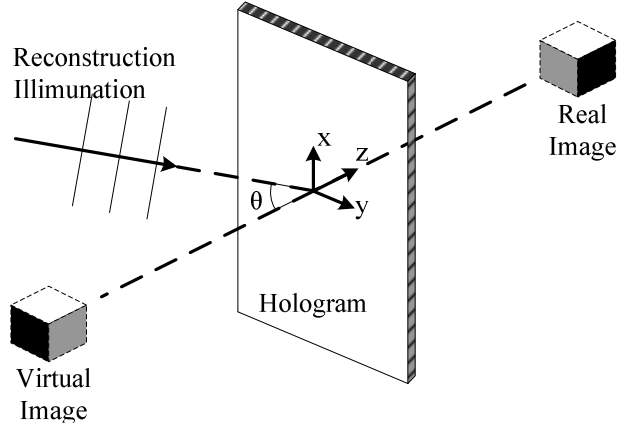


Figure 1.2: Holographic reconstruction scheme

illumination direction, on the other hand it is spatially non-uniform since wavefront amplitude of the object wave is spatially varying. Hence it causes spatial distortions on the other signals. These two terms together are called the zero-order terms. The last signal is the conjugate of the object wave that diffracts to opposite side and direction of the virtual object forming a real image of the object. Twin image or conjugate image are the other synonyms that are used to name this component. This image can be viewed by placing a screen at the correct distance. Another terminology that is used to name the virtual image and the real image is to call them as +1 order image and -1 order image respectively.

In inline holography (where $\theta = 0$) these four terms appear at different physical locations in terms of distance to the hologram plane but they are spatially co-centric. Hence when an inline hologram is viewed from illumination direction, image of the virtual object is distorted by the self interference term $|U_o|^2 U_r$. On the other hand in off-axis holography zero-order terms, virtual object wave and the real object wave diffract to different spatial locations [37]. When a hologram is reconstructed on a computer (digital reconstruction methods are explained in the next chapter) all of the signals are present in the resulting image. For example in the reconstruction result

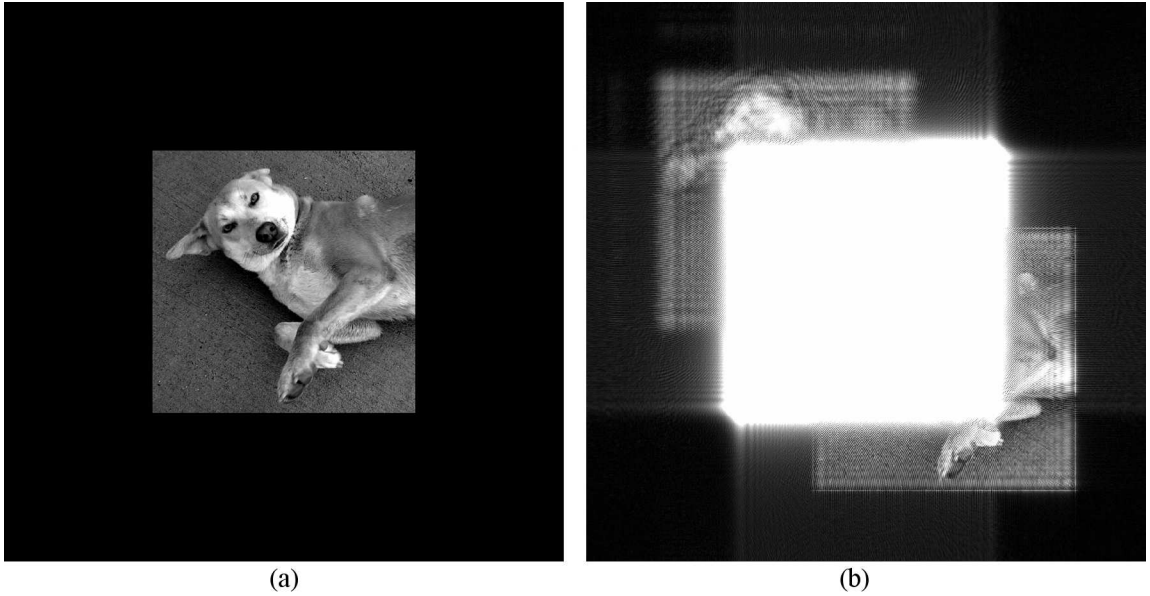


Figure 1.3: (a) Object to be recorded holographically. It is padded with zeros in order to avoid aliasing. (b) Reconstructed off-axis hologram without any filtering. Because of off-axis recording geometry images are not co-centric, i.e. zero-order image is at the center, focused virtual image is at the lower right and defocused real image is at the upper left. Zero-order and the real image partially blocks the virtual image.

shown in Fig. 1.3 the bright part at the center is the zero-order term and occludes the other images. If hologram is reconstructed at the initial distance of the object, virtual image is at focus and the real image is out of focus. In Fig. 1.3 focused virtual image is seen at the lower right and defocused real image is seen in upper left. In addition to the self interference term this out of focus image of the real object also causes distortions on the image of the virtual object. The reverse is also true for real image. If virtual image is wanted to be viewed, then the distorting components must be removed from the reconstruction result. Filtering in holography context means elimination of these components. Here two commonly used filtering techniques are explained and references for further filtering techniques are given.

1.1.1 Filtering With Multiple Captures

Filtering with multiple captures basically uses the idea of capturing unwanted components and subtracting them from the hologram. This intuitive method is compiled in [38]. First, removal of the zero-order images and then removal of the conjugate image are explained.

Filtering Zero-order Images

To do so intensities of the object wave $|U_o|^2$ and the reference wave $|U_r|^2$ are captured and subtracted from the hologram intensity. Filtered hologram I_{hf} will be:

$$I_{hf} = I_h - |U_o|^2 - |U_r|^2 = U_o U_r^* + U_o^* U_r. \quad (1.5)$$

A second method to remove the zero-order is to use phase shifting. When a phase shift of θ is added to the reference wave then hologram intensity with phase shift I_{hp} will be:

$$I_{hp}(\theta) = |U_o|^2 + |U_r|^2 + \exp(i\theta) U_o U_r^* + \exp(-i\theta) U_o^* U_r. \quad (1.6)$$

Subtracting phase shifted hologram from the initial hologram will give:

$$I_{hf}(\theta) = I_h - I_{hp}(\theta) = [1 - \exp(i\theta)] U_o U_r^* + [1 - \exp(-i\theta)] U_o^* U_r. \quad (1.7)$$

The zero-order term is filtered for all values of θ except $\theta = 0$. Maximum intensity for the filtered image is obtained when the phase shift is equal to $\theta = \pi$.

$$I_{hf}(\theta = \pi) = 2(U_o U_r^* + U_o^* U_r). \quad (1.8)$$

Using this method zero-order terms are filtered and reconstruction result is shown in Fig. 1.4

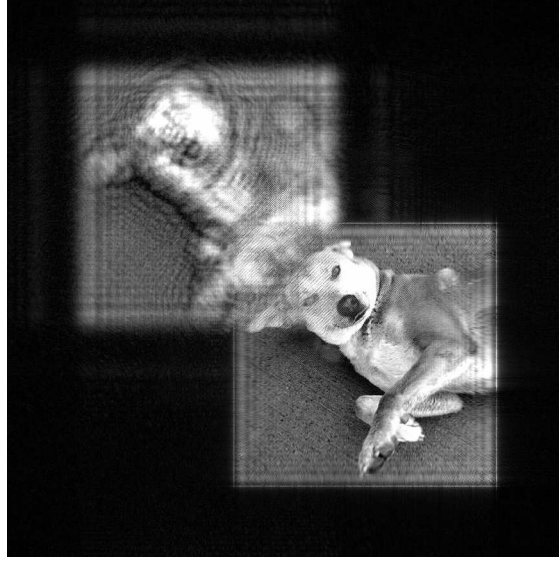


Figure 1.4: Zero-order image is filtered using two phase shifted holograms. Most part of the virtual image is clear but defocused real image again partially blocks the virtual image.

Filtering Zero-order and Conjugate Images

Again there are two methods to filter zero-order and conjugate images. First method is to remove the zero-order using the aforementioned method and then remove the conjugate image using phase shifting.

$$\begin{aligned}
 I_{hf} &= (I_h - I_o - I_r) - \exp(i\theta) (I_{hp} - I_o - I_r) \\
 &= [1 - \exp(i2\theta)] U_o U_r^*
 \end{aligned} \tag{1.9}$$

The magnitude of the $U_o U_r^*$ becomes maximum when the phase shift is $\theta = \pi/2$. The last method that is used to remove both zero-order and conjugate images is the capturing of two phase shifted holograms $I_{hp}(\theta_1)$ and $I_{hp}(\theta_2)$ such as:

$$\begin{aligned}
 I_{hp}(\theta_1) &= |U_o|^2 + |U_r|^2 + \exp(i\theta_1) U_o U_r^* + \exp(-i\theta_1) U_o^* U_r, \\
 I_{hp}(\theta_2) &= |U_o|^2 + |U_r|^2 + \exp(i\theta_2) U_o U_r^* + \exp(-i\theta_2) U_o^* U_r.
 \end{aligned} \tag{1.10}$$

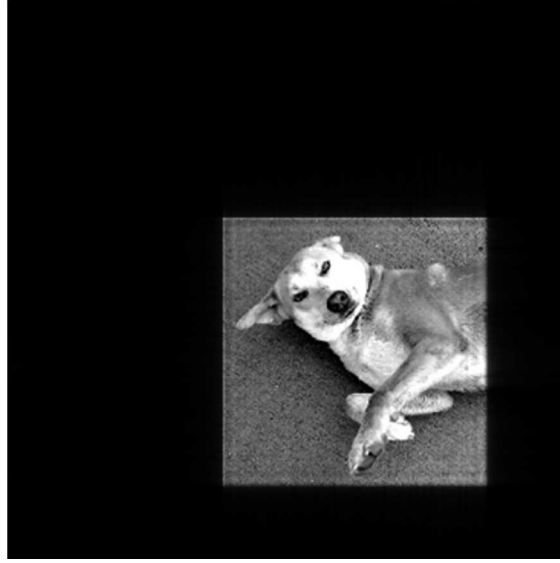


Figure 1.5: Zero-order and the conjugate images are filtered using phase shifted holograms.

Then using I_h , $I_{hp}(\theta_1)$ and $I_{hp}(\theta_2)$ filtered hologram is obtained by:

$$\begin{aligned}
 I_{hf} &= \exp(i\theta_1)I_{hp}(\theta_1) - \exp(-i\theta_2)I_{hp}(\theta_2) + [\exp(i\theta_1) + \exp(-i\theta_2)] I_h \\
 &= \left[\frac{\exp(i\theta_1) - 1}{\exp(-i\theta_1) - 1} - \frac{\exp(i\theta_2) - 1}{\exp(-i\theta_2) - 1} \right] U_o U_r^*.
 \end{aligned} \tag{1.11}$$

The filtered image intensity becomes maximum when $\theta_1 = 2\pi/3$ and $\theta_2 = -2\pi/3$. The reconstruction results is shown in Fig. 1.5.

To implement these methods it is needed to capture multiple images, at least three captures. This makes the methods not implementable in real-time. In the literature there are methods offered to make the process practical with less number of captures. Parallel phase-shifting methods offered in [39–41] carries the phase shifting operations in real time using a phase-shifting array device. On the other hand the usage of the phase shifting device and the lens introduces aberrations. Most importantly, strict requirement of alignment makes the method impractical although initial experimental results are presented in the papers. Another example of filtering

using phase shifting is given in [42]. Method offers to add phase difference to each orthogonal polarization and then to obtain the filtered result with usage of the image of the object. The need for pre-captured image of the object makes this method not applicable for moving objects. Last phase-shifting method uses again the parallel phase shifting scheme with small modifications [43]. In this method intensity of the reference wave should be known and kept sufficiently high with respect to object wave. Hence with proper adjustment of reference wave during recording, filtered holograms of the moving objects can be recorded.

1.1.2 Spatial Filtering

First of all, spatial filtering builds up on the spatial separation of the signals in a hologram. Hence it is only applicable in the off-axis holography [44]. Previously a reference wave that makes angle of θ with the hologram plane normal was represented as in Eq. 1.1. Then the hologram intensity can be rewritten in the expanded form:

$$I_h(x, y) = |U_o|^2 + |U_r|^2 + U_o|U_r| \exp(-ikx \sin \theta) + U_o^*|U_r| \exp(ikx \sin \theta). \quad (1.12)$$

Hence when the hologram is reconstructed with a wave U of uniform phase, the phase multiplier $\exp(-ikx \cos \theta)$ of the third term indicates that the wave is propagating with an angle of $-\theta$ with respect to U . The phase factor at the fourth term indicates a diffraction with an angle of θ . If the Fourier transform of the hologram is taken the phase factors will give spatial frequency shift in the 2D frequency spectrum. Frequency components of the virtual image and the real image will lie at symmetric locations $[-k \sin(\theta/2)]$ and $[k \sin(\theta/2)]$ respectively. Then using band-pass filtering zero-order and twin images can be eliminated.

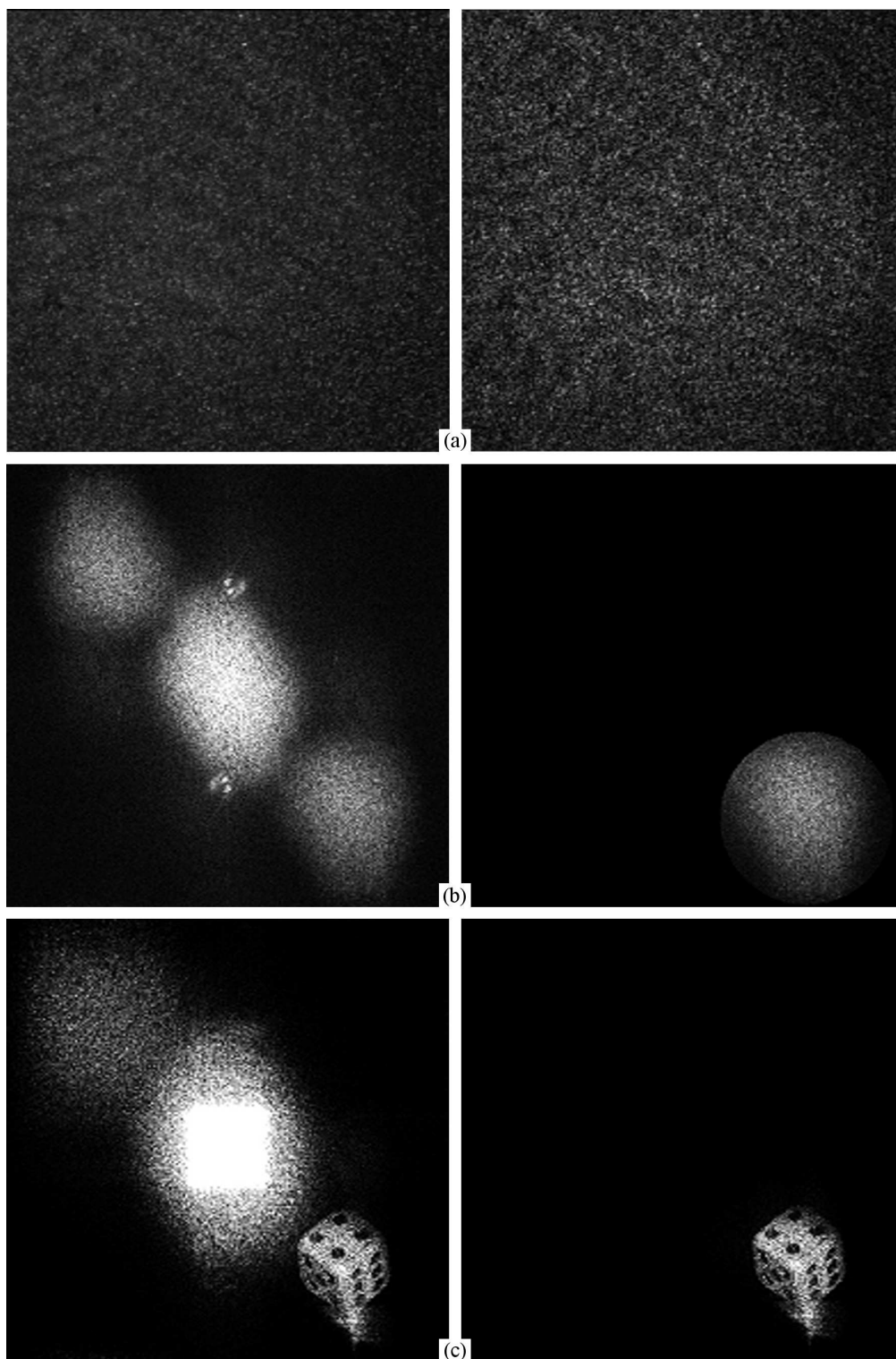


Figure 1.6: In this figure an experimentally recorded hologram of a dice is seen. Left column consists of unfiltered holograms and right column consists of filtered holograms. (a) Recorded off-axis hologram and filtered hologram. (b) Frequency spectrum of the holograms. (c) Reconstruction results.

Application of the method is shown in Fig. 1.6 for an off-axis hologram of a dice. The recording distance was $0.7m$. In the figure captured hologram, its frequency components and reconstruction results are shown. It can be seen that frequency components are separated well. Frequency components for the zero-order, the virtual image and the real image can be seen at the center, lower right and upper left of the frequency spectrum respectively. Also the frequency components of multiple reflections can be seen just above and below the zero-order components. A band-pass filtering (circular windowing) is applied to remove frequency components of the zero-order and the real image. Here a simple circular windowing is applied but various windows such as Hamming, Tukey or Gaussian can be used accordingly. Then an inverse Fourier transform is applied to this frequency spectrum to obtain filtered hologram. When this hologram is reconstructed, the result is free of the zero-order and the real image as shown in Fig. 1.6.

Before passing to other methods that utilize different signal processing concepts it should be noted that implementation of the spatial filtering can be done in quite different ways. For example in [45], Pedrini implements the method on an experimental setup with different masks for microscopy applications. In a different way Zhang implemented the method with a grating to remove zero-order diffraction in [46]. The methods explained here can be classified as introductory methods for the filtering topic in holography. Other methods are briefly given in the next section for the people who are interested.

1.1.3 Other Filtering Techniques

When a deep investigation of the holography process is done, it can be seen that holography is a fertile area to apply the methods that is used in signal processing and optics. Liebling considered the well known wavelets for diffraction in the holography process and designed a new wavelet bases called Fresnelets in [47]. Then an obvious extension of the Fresnelets is to use them in filtering. Same researchers filtered zero-order and real image terms by suppressing their corresponding Fresnelet coefficients in [48]. An enhancement over spatial filtering is reported when the Fresnelets are used. For the filtering in in-line holography an earlier method proposed by Onural must be noted [49]. Onural modeled the reconstruction process as a linear space-invariant system and developed an iterative algorithm. The algorithm relies on setting up a recursive relation between real part and imaginary part of the free-space impulse response. In [50] Kim proposes an adjustment to the filter coefficients in frequency domain for digital implementation of Onural's algorithm.

2 DIGITAL HOLOGRAPHY RECONSTRUCTION METHODS

Originally holograms were recorded on photographic films or photographic plates which required tedious process of development before they are ready for reconstruction [16]. Thermoplastic materials enabled real time processing [51] but the breakthrough was after the rapid developments in digital electronics, especially charge-coupled device (CCD) based cameras. CCD cameras made it possible to record the holograms digitally [33]. The recorded intensity data is ready for processing on a computer hence hologram reconstruction is started to be done on computers numerically without any laser light illumination. Hologram reconstruction methods can also be used to create diffraction patterns or object waves projecting from computer synthesized object [52,53]. Hence the numerical hologram reconstruction methods in terms of accuracy and speed became an important research area.

This chapter is about the numerical reconstruction of digital holograms. To do so discrete implementation of the wave propagation is explained in detail and we clarify the inconsistencies in the literature. The wave propagation is used first for digital hologram reconstruction and then for creating CGH of virtual computer objects [34].

2.1 Diffraction Calculation

In order to reconstruct a digital hologram numerically it is needed to calculate the diffracted wave field from hologram. Wave field distribution $U_0(x, y)$ as shown in Fig. 2.1 in the (x, y) plane - object plane - will create a wave field $U_0(\xi, \eta)$ at an

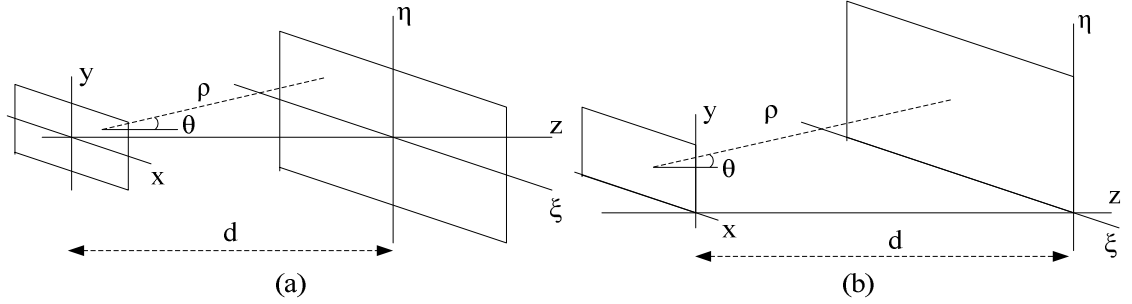


Figure 2.1: Left: Coordinate system used in derivation of Fresnel diffraction equation, both planes are centered around zero. Right: As it is explained in the text if bounds of the summations are set to start from zero without properly shifting the indices, the diffraction integral is calculated in this coordinate system.

observation plane (ξ, η) that is related with Rayleigh-Sommerfeld diffraction integral [37]:

$$U(\xi, \eta) = \frac{1}{i\lambda} \int_{-\infty}^{\infty} \int_{-\infty}^{\infty} U_0(x, y) \frac{\exp(-ik\rho)}{\rho} \cos \theta \, dx \, dy, \quad (2.1)$$

where $\rho = \sqrt{d^2 + (x - \xi)^2 + (y - \eta)^2}$ is the Cartesian distance between the points on the object plane and the observation plane, $k = 2\pi/\lambda$ is the wave number, and $\cos \theta$ is the obliquity factor and it is $\cos \theta \approx 1$ in most cases [37].

2.1.1 Fresnel Transform

For the distances d that are large compared to dimensions of the object, the ρ in the denominator of the diffraction equation can be approximated as d whereas it is not true for the numerator. Small deviations of ρ may produce large errors at the object wave result since it is in the phase term. So a higher order approximation is done by taking first two terms of the binomial expansion of ρ :

$$\rho \approx d + \frac{(x - \xi)^2}{2d} + \frac{(y - \eta)^2}{2d} \quad (2.2)$$

is substituted in the numerator. Now the diffraction integral is in its so-called Fresnel transform representation [37, 54]:

$$\begin{aligned}
U(\xi, \eta) &= \frac{1}{i\lambda d} \exp(-ikd) \exp \left[-i\frac{k}{2d}(\xi^2 + \eta^2) \right] \\
&\times \int_{-\infty}^{\infty} \int_{-\infty}^{\infty} U_0(x, y) \exp \left[-i\frac{k}{2d}(x^2 + y^2) \right] \exp \left[i\frac{k}{d}(x\xi + y\eta) \right] dx dy.
\end{aligned} \tag{2.3}$$

In this equation the wave field is simply a two dimensional inverse Fourier transform of the field $U_0(x, y)$ multiplied by a quadratic phase factor [37, 54]. For numerical calculation of the diffraction integral it is required to derive the discrete form of the diffraction integral. Suppose the object plane is represented by $N_x \times N_y$ grid with step sizes of Δx and Δy along the x and y directions, the observation plane is also represented with the same number of points (but with the step sizes of $\Delta \xi$ and $\Delta \eta$), a discrete form of the Fresnel transform is obtained:

$$\begin{aligned}
U(m\Delta\xi, n\Delta\eta) &= \frac{1}{i\lambda d} \exp \left(-i\frac{2\pi}{\lambda}d \right) \exp \left[-i\frac{\pi}{\lambda d} (m^2\Delta\xi^2 + n^2\Delta\eta^2) \right] \\
&\times \sum_{k=-N_x/2}^{N_x/2-1} \sum_{l=-N_y/2}^{N_y/2-1} U_0(k\Delta x, l\Delta y) \exp \left[-i\frac{\pi}{\lambda d} (k^2\Delta x^2 + l^2\Delta y^2) \right] \\
&\times \exp \left[i\frac{2\pi}{\lambda d} (k\Delta x m\Delta\xi + l\Delta y n\Delta\eta) \right].
\end{aligned} \tag{2.4}$$

Here k and m are integers between $(-N_x/2)$ and $(N_x/2 - 1)$, similarly l and n are integers between $(-N_y/2)$ and $(N_y/2 - 1)$. From the Fourier transform step sizes in the object plane and the observation plane are related by:

$$\begin{aligned}
\Delta\xi &= \frac{\lambda d}{N_x \Delta x}, \\
\Delta\eta &= \frac{\lambda d}{N_y \Delta y}.
\end{aligned} \tag{2.5}$$

Now, by substituting $\Delta\xi$ and $\Delta\eta$ into Eq. 2.4 we obtain:

$$\begin{aligned}
U(m, n) &= \frac{1}{i\lambda d} \exp\left(-i\frac{2\pi}{\lambda}d\right) \exp\left[-i\pi\lambda d\left(\frac{m^2}{N_x^2\Delta x^2} + \frac{n^2}{N_y^2\Delta y^2}\right)\right] \\
&\times \sum_{k=-N_x/2}^{N_x/2-1} \sum_{l=-N_y/2}^{N_y/2-1} U_0(k, l) \exp\left[-i\frac{\pi}{\lambda d}(k^2\Delta x^2 + l^2\Delta y^2)\right] \\
&\times \exp\left[i2\pi\left(\frac{k m}{N_x} + \frac{l n}{N_y}\right)\right].
\end{aligned} \tag{2.6}$$

Ignoring the constant terms before the exponential this equation can be written in a more compact form as:

$$U(m, n) = Q_i(m, n) \sum_{k=-N_x/2}^{N_x/2-1} \sum_{l=-N_y/2}^{N_y/2-1} U_0(k, l) Q_o(k, l) \exp\left[i2\pi\left(\frac{k m}{N_x} + \frac{l n}{N_y}\right)\right] \tag{2.7}$$

where

$$\begin{aligned}
Q_i(m, n) &= \exp\left[-i\pi\lambda d\left(\frac{m^2}{N_x^2\Delta x^2} + \frac{n^2}{N_y^2\Delta y^2}\right)\right], \\
Q_o(k, l) &= \exp\left[-i\frac{\pi}{\lambda d}(k^2\Delta x^2 + l^2\Delta y^2)\right].
\end{aligned} \tag{2.8}$$

Basically Eq. 2.7 is a two dimensional inverse discrete Fourier transform (IDFT) multiplied with quadratic terms. At this point calculation of this IDFT requires proper handling. This could be a confusing issue as in some of the literature [33, 55]. Generally the double sum with the IDFT kernel in Eq. 2.7 is immediately written using IDFT notation [54, 56] as:

$$U(m, n) = Q_i(m, n) \mathcal{F}\mathcal{F}\mathcal{T}^{-1} \{U_0(k, l) Q_o(k, l)\}, \tag{2.9}$$

where $\mathcal{F}\mathcal{F}\mathcal{T}^{-1}$ is used to denote the fast Fourier transform which is generally used for efficient DFT calculations. Here if we remind the forward and the inverse discrete

Fourier transform relations respectively:

$$\begin{aligned}
X(k, l) &= \sum_{m=0}^{N_x-1} \sum_{n=0}^{N_y-1} x(m, n) \exp \left[-i2\pi \left(\frac{k m}{N_x} + \frac{l n}{N_y} \right) \right] \\
x(m, n) &= \frac{1}{N_x N_y} \sum_{k=0}^{N_x-1} \sum_{l=0}^{N_y-1} X(k, l) \exp \left[+i2\pi \left(\frac{k m}{N_x} + \frac{l n}{N_y} \right) \right],
\end{aligned} \tag{2.10}$$

we would notice that bounds of the double sum in these equations start from 0 and ends up at $(N_x - 1)$ and $(N_y - 1)$. Hence Eq. 2.9 is not quite true since bounds of the double sum in Eq. 2.6 runs from $(-N_x/2)$ to $(N_x/2 - 1)$ and $(-N_y/2)$ to $(N_y/2 - 1)$. This can be understood better from the illustration in Fig. 2.1. The derivation of the discrete Fresnel transform in Eq. 2.7 is done using the coordinate system shown on the left where as in Eq. 2.9 it is misleadingly assumed to be done using the coordinate system shown on the right. Therefore a shift operation in the indices k, l, m, n is vital. There are two different correct ways to shift the indices and evaluate the Fresnel transform as it is explained below.

Method 1

Now, lets introduce dummy variables k', l', m', n' such that

$$k = (k' - N_x/2), \quad l = (l' - N_y/2), \quad m = (m' - N_x/2), \quad n = (n' - N_y/2), \tag{2.11}$$

and substitute them into Eq. 2.7:

$$U(m, n) = Q'_i(m, n) \sum_{k=0}^{N_x-1} \sum_{l=0}^{N_y-1} U_0(k, l) Q'_o(k, l) \exp \left[i2\pi \left(\frac{k m}{N_x} + \frac{l n}{N_y} \right) \right]. \tag{2.12}$$

where $Q'_i(m, n)$ and $Q'_o(k, l)$ are given as:

$$\begin{aligned}
Q'_i(m, n) &= \exp \left[i\pi \frac{(N_x + N_y)}{2} \right] \exp [-i\pi(m + n)] Q_i \left[m - \frac{N_x}{2}, n - \frac{N_y}{2} \right], \\
Q'_o(k, l) &= \exp [-i\pi(k + l)] Q_o \left[k - \frac{N_x}{2}, l - \frac{N_y}{2} \right].
\end{aligned} \tag{2.13}$$

Therefore, discrete Fresnel transform can be evaluated correctly with its modified version below:

$$U(m, n) = Q'_i(m, n) \mathcal{F}\mathcal{F}\mathcal{T}^{-1} \{U_0(k, l) Q'_o(k, l)\}, \quad (2.14)$$

In passing, one can calculate discrete form of the diffraction equation (Eq. 2.6) by carrying out the double sum without FFT but computation complexity will boost from $\mathcal{O}(N^2 \log N)$ to $\mathcal{O}(N^4)$ for an $N \times N$ array.

Method 2

Especially for the ones that use Matlab software there is a more easy way to do the shift operation. Since discrete Fourier transform is a cyclic operation, namely $U(m + \alpha N_x, n + \beta N_y) = U(m, n)$ holds for any integers α and β , one can also calculate the diffracted field pattern as:

$$U(m, n) = Q_i \left(m - \frac{N_x}{2}, n - \frac{N_y}{2} \right) \times \mathcal{S} \left\{ \mathcal{F}\mathcal{F}\mathcal{T}^{-1} \left\{ \mathcal{S} \left[U_0(k, l) Q_o \left(k - \frac{N_x}{2}, l - \frac{N_y}{2} \right) \right] \right\} \right\}, \quad (2.15)$$

where \mathcal{S} operator does shift in the indices. It moves the zero-frequency component to the center of the array in one dimensional Fourier transform. In 2D arrays it swaps the first quadrant with the third and the second quadrant with the fourth of a matrix. This operation can be carried out in any coding environment but it is the `fftshift` function in Matlab.

2.1.2 Convolution Method

An alternative way of implementing the Rayleigh-Sommerfeld diffraction integral is the convolution approach. If we model the propagation of light in free space as a

linear system then diffraction integral can also be written as a convolution integral:

$$U(\xi, \eta) = \int_{-\infty}^{\infty} \int_{-\infty}^{\infty} U_0(x, y) h(\xi, \eta, x, y) dx dy, \quad (2.16)$$

where $h(\xi, \eta, x, y)$ is the impulse response of the free space given as [54, 55]

$$h(\xi, \eta, x, y) = \frac{i}{\lambda} \frac{\exp \left[-i \frac{2\pi}{\lambda} \sqrt{d^2 + (x - \xi)^2 + (y - \eta)^2} \right]}{\sqrt{d^2 + (x - \xi)^2 + (y - \eta)^2}}, \quad (2.17)$$

with the $\cos \theta \approx 1$ approximation as usual. The discrete version of the impulse function immediately follows:

$$h(k, l) = \frac{i}{\lambda} \frac{\exp \left[-i \frac{2\pi}{\lambda} \sqrt{d^2 + \left(k - \frac{N_x}{2}\right)^2 \Delta x^2 + \left(l - \frac{N_y}{2}\right)^2 \Delta y^2} \right]}{\sqrt{d^2 + \left(k - \frac{N_x}{2}\right)^2 \Delta x^2 + \left(l - \frac{N_y}{2}\right)^2 \Delta y^2}}. \quad (2.18)$$

In this equation a shift of the coordinates by $N_x/2$, $N_y/2$ are done to use the coordinate system on the left in Fig. 2.1. Convolution operation can be carried out using double sum but it has computational load of $\mathcal{O}(N^4)$. Since according to the convolution theorem the convolution of two functions can be calculated using Fourier transform. Convolution operation is equal to the inverse Fourier transform of the product of each function's individual Fourier transforms. Then one can also calculate the diffracted field as:

$$U(m, n) = \mathcal{S} \left\{ \mathcal{F}\mathcal{F}\mathcal{T}^{-1} \left[\mathcal{F}\mathcal{F}\mathcal{T}(U_0(k, l)) \mathcal{F}\mathcal{F}\mathcal{T}(h(k, l)) \right] \right\} \quad (2.19)$$

The complexity of the DFT (FFT) based approach is on the order of three FFT calculations instead of $\mathcal{O}(N^4)$ of direct linear convolution approach. Also number of FFT operations can be reduced by one if one can calculate the DFT of $h(k, l)$ analytically.

In addition to the complexity there is another conceptual difference between direct linear convolution approach and the convolution with FFT approach. The size of diffraction pattern calculated by direct linear convolution is $(2N - 1) \times (2N - 1)$ pixels for input object size of $N \times N$ pixels and the central $N \times N$ pixels of the resultant image is the actual result. However in FFT based convolution approach if there is nothing done prior to the FFT, the convolution operation with FFT will not produce $(2N - 1) \times (2N - 1)$ pixels image but $N \times N$ pixels image. This is because the FFT operation is cyclic and the result will be the circular convolution of two functions, however what we need is the linear convolution of them. To properly carry out the linear convolution operation input image has to be padded with zeros to bring the input image size to $(2N - 1) \times (2N - 1)$ pixels (similarly the size of $h(k, l)$ has to be padded with zeroes to bring the size of $h(k, l)$ to $(2N - 1) \times (2N - 1)$ pixels. Then the calculation with FFT method will produce again $(2N - 1) \times (2N - 1)$ pixel image result and again the central $N \times N$ portion of the image is the actual result. Then computational complexity of the convolution method with FFT is $\mathcal{O}[(2N - 1)^2 \log_2(2N - 1)]$.

If we compare Fresnel transform and the convolution method there is a fundamental difference in the pixel sizes. In convolution approach the reconstructed pixel size is equal to the input pixel size, i.e.;

$$\Delta\xi = \Delta x \quad \text{and} \quad \Delta\eta = \Delta y,$$

whereas in Fresnel approximation the pixel sizes are different on the object plane and the recording plane as can be deduced from Eq. 2.5. This means that the reconstruction of the a hologram with convolution approach could be magnified or demagnified version of the one calculated by Fresnel approximation [54]. Since the pixel dimensions do not change with the convolution approach, the reconstruction size is constant over distance d and this property finds applications in numerical reconstruction of holograms of particle distribution in transparent mediums [54].

2.2 Numerical Results

In this section we present comparative reconstruction results for experimentally recorded holograms and calculations for CGH's of computer synthesized objects using Fresnel transform and the convolution approach. In the experimental set up, a 30 mW HeNe laser light is divided in to two arms and one arm is passed through a pinhole and collimated to be assumed as a plane wave which is used as reference wave. An off-axis hologram of a dice placed approximately 89 *cm* away from the CCD array is recorded. The CCD had a (1534×1024) array of $9 \mu m \times 9 \mu m$ size pixels. Figure 2.2 shows the actual recorded hologram, numerical reconstructed amplitude and phase of the holograms at a reconstruction distance of 89 *cm*. The first reconstruction result is calculated by Eq. 2.7 by taking the summation limits starting from 0 to N_x and N_y . The second and the third hologram reconstruction results were calculated by the corrected versions of the discrete diffraction equations, namely by using Eq. 2.14 and Eq. 2.15 respectively. As it is clearly seen from these images, uncorrected form of the equation produces incorrect view of the object wave; the location of object wave, its conjugate and the location of the zero order waves are shifted. At first sight it might seem that with some shifting operation correct view can be obtained and there is no information is lost due to cyclic property of discrete Fourier transform. The following example will show that this may be true only in cases where the quadrature terms are insignificant otherwise there will be a visible distortion in the reconstructed images.

We know that evaluating the diffraction integral using Eq. 2.9 will result a spatial shift in the observation plane. Hence one can say that if we use the diffraction integral two times in succession - first to calculate the CGH and second to calculate the recon-

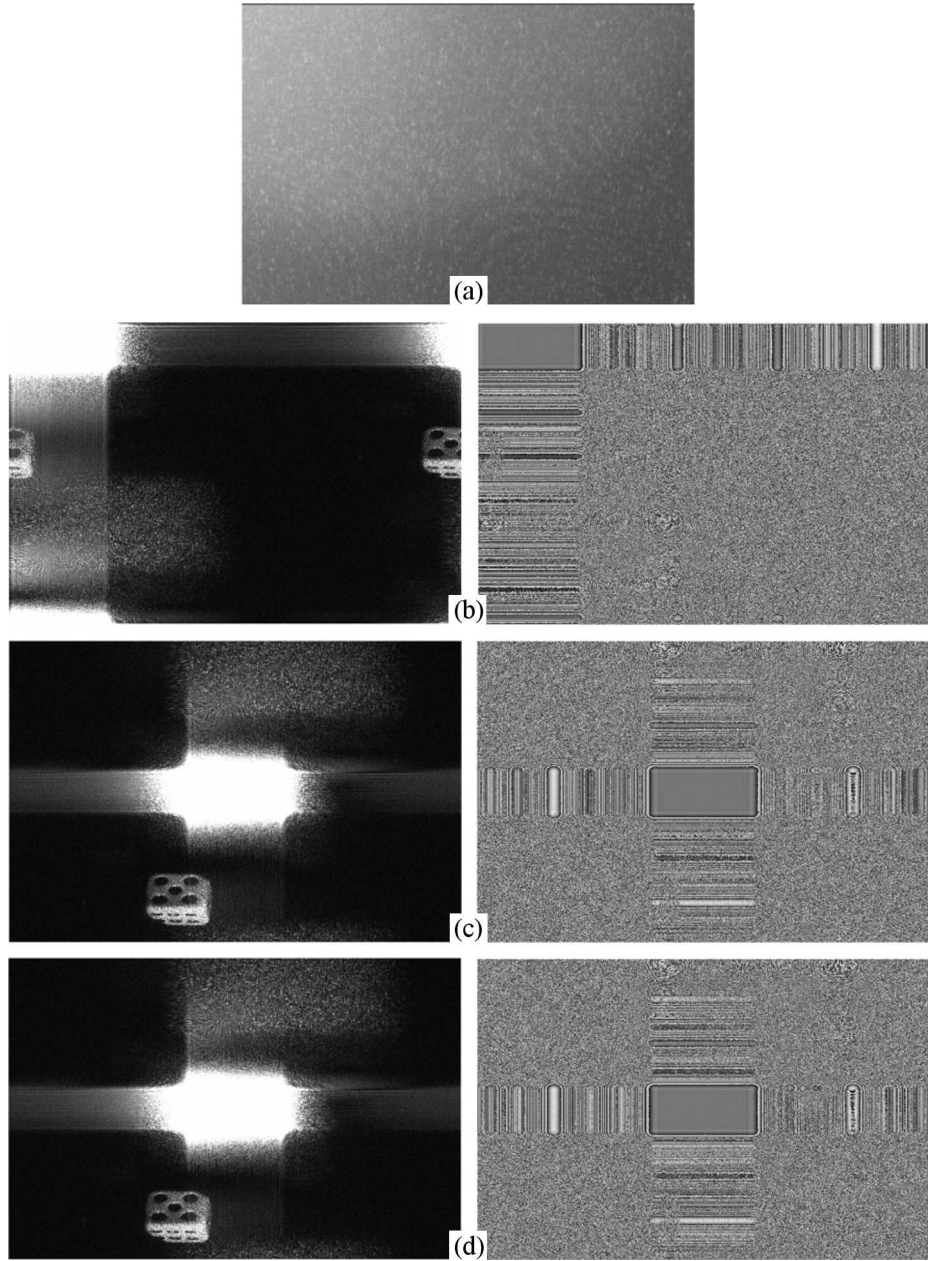


Figure 2.2: (a) 1534×1024 pixels hologram of a dice recorded in off-line configuration with a 30 mW HeNe laser. The pixel dimensions are $9 \mu\text{m} \times 9 \mu\text{m}$ and the object distance d is 89 cm . (b) Amplitude and phase of the reconstructed hologram that is computed using Eq. 2.9. The image of the object is not at the right place. (c) Amplitude and phase of the reconstructed hologram by Method 1, using Eq. 2.14 and finally, (d) Amplitude and phase of the reconstructed hologram by Method 2, using Eq. 2.15. Last two methods produce exactly the same results as expected. Note that the actual pixel dimensions in the reconstructed image is different (ratio of vertical-pixel size to horizontal-pixel size is $1534/1024$) as given by Eq. 2.5 which means that the physical size of the reconstructed holograms is same in both vertical and horizontal directions. Here we show the pixel values so the reconstructed holograms look like the same size as the hologram.

struction result - we will have the recorded object image in correct spatial locations since the FFT operation is cyclic. This justification might seem correct but we will see in the following example that object image is at the correct place but there are errors in the result. In this example, a planar picture is numerically propagated using Fresnel transform and its CGH is created by adding a uniform plane wave to the object wave. Then zero-order image is filtered using phase shifting and then the filtered hologram is reconstructed. Reconstruction results for different recording distances are shown in Fig 2.3. In this figure, reconstruction results calculated using the correct version of the diffraction equation (Eq. 2.15) and by using Eq. 2.9 are shown on the top and bottom row subfigures respectively. At $d = 1.0\text{ m}$ reconstruction results with the correct or uncorrect versions of the Fresnel transform seems not to differ. At shorter reconstruction distances ($d = 0.9\text{ m}$ and $d = 0.8\text{ m}$) again objects appear at the correct locations but there are severe distortions on the image calculated using uncorrected version. The corrected version gives clean virtual images at all distances.

In a different simulation far field patterns calculated by the corrected discrete Fresnel transform and the far field patterns calculated by the convolution method are compared. Convolution calculations are implemented via FFT routines and as it was previously explained. The calculated field dimensions in the observation plane changes according to Eq. 2.5 for the Fresnel transform, but it does not change for the convolution method. For example in Fig. 2.4 a 256×256 image with pixel dimensions of $30\mu\text{m} \times 30\mu\text{m}$ is taken as the object and it is propagated using Fresnel transform and the convolution method. The same calculation for the previous 256×256 image is carried out again but it is padded with zeros up to dimensions of 512×512 . The simulation results can be seen in the Fig. 2.5.

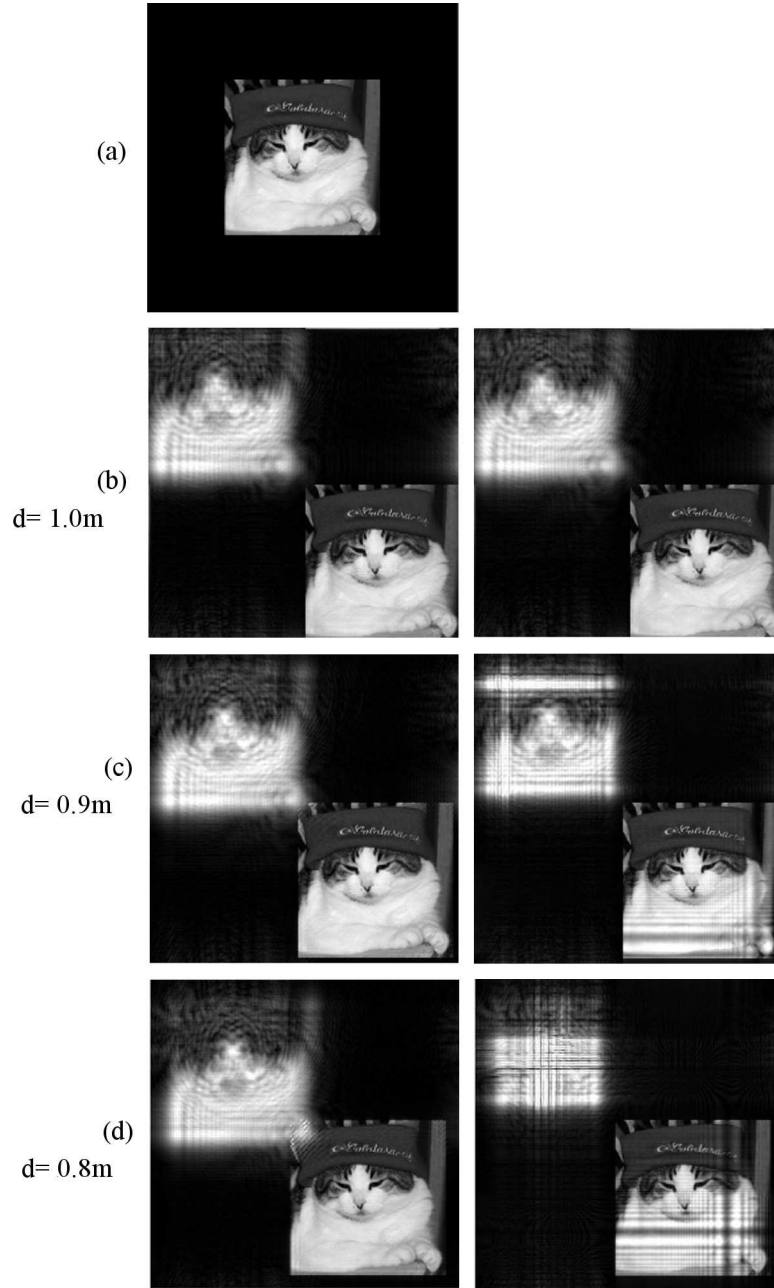


Figure 2.3: An example of computer generated holography. From the 512×512 planar object shown (Yumoş, the cat with a hat) in (a) off-axis holograms were calculated using Fresnel diffraction equation at three different distances with a reference wave that has 0.3° angle with both transverse axes. The pixel dimension of the image is taken as $40\mu\text{m} \times 40\mu\text{m}$. Then using phase shift holography method to remove the zero order term object is reconstructed where (b), (c), and (d) shows the magnitude of reconstructed holograms. Left column is calculated by using the correct version of the diffraction equation (Eq. 2.15) and the right column is calculated using Eq. 2.9. As the distance decreases the effect of the quadrature terms become more significant and it is the reason for the distortion seen in the bottom row images.

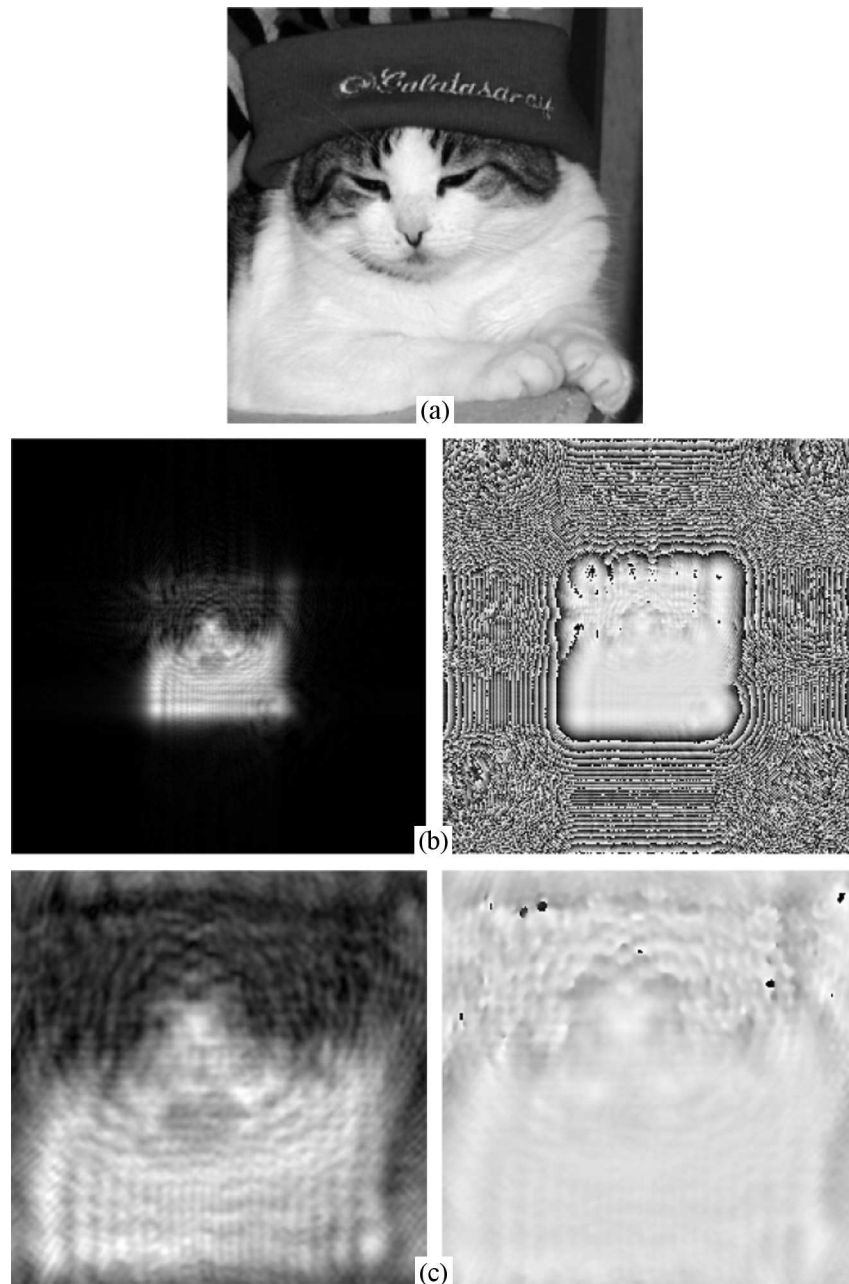


Figure 2.4: (a) A (256 by 256) input image, pixel dimensions are assumed to be $30\mu m \times 30\mu m$. (b) Far field magnitude and phase plots for $d = 1 m$ calculated by the correct discrete Fresnel equation, pixel size $82\mu m \times 82\mu m$, (c) Far field magnitude and phase plots for $d = 1 m$ calculated by the convolution approach (Eq. 2.19). In convolution calculation zeroes are padded around the image to prevent the aliasing as it is explained in the text, here we show the central 256×256 pixels of the resulting image. We see $\approx 82/30$ times magnified portion of the far field distribution with the convolution approach as expected. For this example with a 1.75 GHz Pentium PC, discrete Fresnel approximation calculation by FFT takes ≈ 0.22 sec, convolution via FFT takes ≈ 1.48 sec and direct convolution is ≈ 30 sec (not shown) using Matlab software.

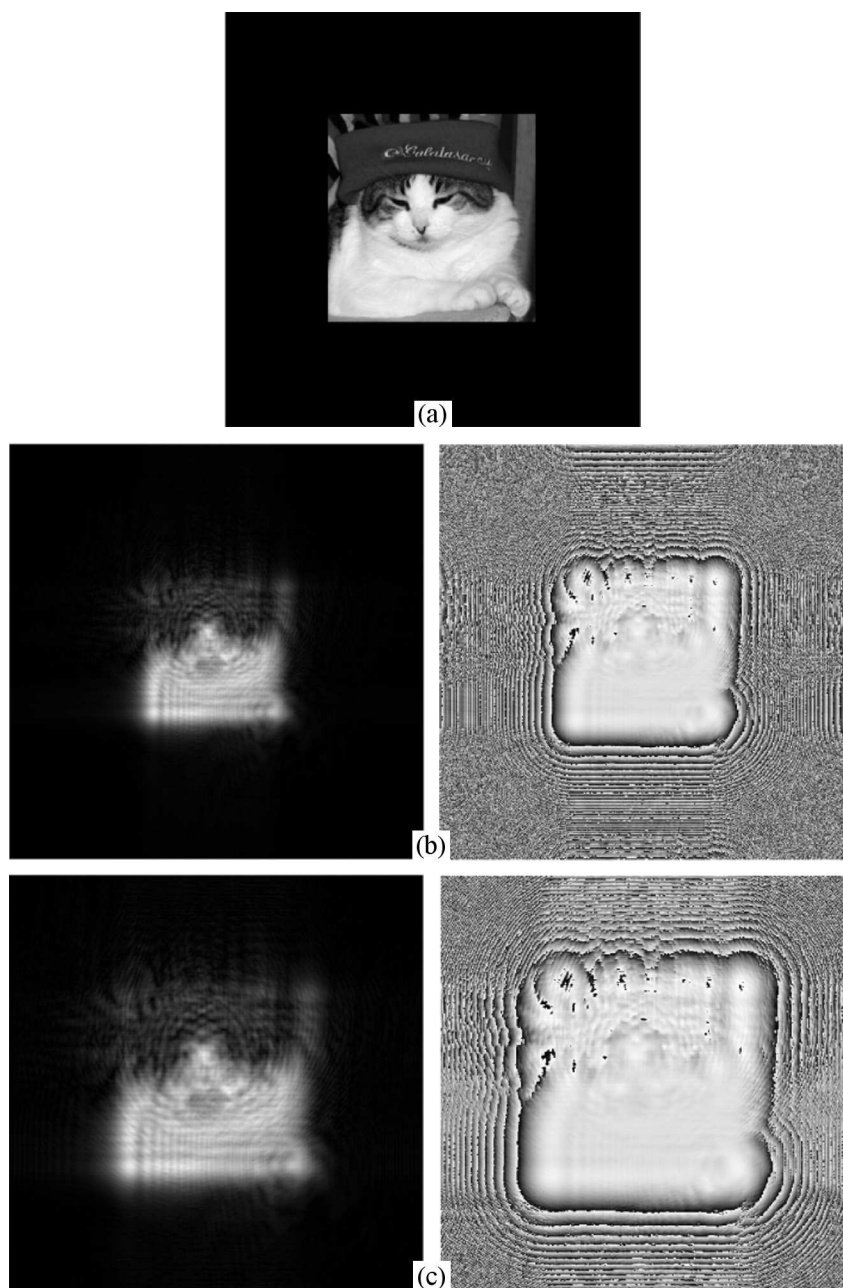


Figure 2.5: (a) A (512 by 512) input image, pixel dimensions are assumed to be $30\mu m \times 30\mu m$. (b) Far field magnitude and phase plots for $d = 1 m$ calculated by the correct discrete Fresnel equation, pixel size $41\mu m \times 41\mu m$, (c) Far field magnitude and phase plots for $d = 1 m$ calculated by the convolution approach (Eq. 2.19). In convolution calculation zeroes are padded around the image to prevent the aliasing as it is explained in the text, here we show that the central 512×512 pixels of the resulting image. We see $\approx 41/30$ times magnified portion of the far field distribution with the convolution approach as expected. For this example with a 1.75 GHz Pentium PC, discrete Fresnel approximation calculation by FFT takes ≈ 0.89 sec, convolution via FFT takes ≈ 11 sec and direct convolution is ≈ 480 sec (not shown) using Matlab software.

3 A METHOD FOR COMPUTER GENERATED HOLOGRAPHY

In the previous chapter, Fresnel transform and convolution method are given as two methods for reconstruction of digital holograms. Also these methods are used to calculate the CGH of the cat picture in Fig. 2.3. The picture was a 2D data but for various applications CGH's of computer synthesized 3D objects is required. Hence it is important to find fast and accurate methods to calculate object wave distributions at a distance so the computer generated holograms of objects. In this chapter a literature survey of existing methods is presented and then they are compared in terms of computational complexity. Later a simple, approximate but a fast method -which we call Planar Layers Method (PLM)- is proposed. PLM is compared with the revised methods in terms of speed and an error analysis is carried out to explore its accuracy.

To calculate the diffraction pattern of a 3D object on a finite hologram aperture, intuitive idea will be to calculate the wave field contribution of each point of the object using discretized Rayleigh-Sommerfeld equation (Eq. 2.1) and then to superpose the results. For discrete implementation of Eq. 2.1, object plane and the hologram plane must be sampled. When the object points are bounded and sampled over an $N \times N$ grid there will be N^2 components to be propagated. Similarly if the recording plane is bounded - hologram aperture in our case - and sampled with an $N \times N$ grid then computational complexity of overall calculation will be $\mathcal{O}(N^4)$. This method is called pointwise propagation method (PPM) [57] and it does not make any approximations, therefore result of this method will be taken as the reference for accuracy.

As previously explained diffraction can be modeled as a linear system. Hence we have represented diffraction as a convolution operation in Eq. 2.16 with its impulse response as in Eq. 2.17. The convolution operation can be implemented efficiently by FFT routines as in Eq. 2.19. For this equation, possibility of precalculating the Fourier transform of the free-space impulse response will reduce one of the Fourier transform operations. Then for an $N \times N$ sample, knowing that the complexity of the 2D Fourier transform is $\mathcal{O}(N^2 \log N)$, the complexity of this equation will be $2\mathcal{O}(N^2 \log N) + 2\mathcal{O}(N^2)$ [58]. Here we should note that in order to avoid aliasing, input object intensity distribution and the free space impulse response must be padded with zeros up to the size of the convolution operation, i.e. $(2N - 1) \times (2N - 1)$ and then central $N \times N$ portion of the image will be our actual result.

Another system level approach to diffraction is called the angular spectrum method. In this method angular spectrum components of the input object wave and different operations such as rotation, shift or tilt in the space is considered. Basically angular spectrum is the Fourier domain representation of the signals. The method is introduced by Ganci in order to calculate the diffraction pattern of a slit between parallel planes as usual, but the wave has a tilt with respect to planes [59]. Later Patorski calculated the diffraction patterns between plane apertures when only the source plane has a tilt [60]. Both of these methods use Fraunhofer approximation. Rabal [61] introduced utilization of Fourier transform and Leseberg [62, 63] introduced usage of Fresnel approximation for the field calculations of tilted planes. Later the studies in this area are advanced by Tomassi and Bianco's works in which they set up a connection between plane wave spectrums of rotated planes and its applications in CGH [64–66]. Then Delen and Hooker lifted up the Fraunhofer and the

Fresnel approximation limitations and come out with a method for full-scalar diffraction [67]. Matsushima et. al. used various interpolation algorithms to setup the same full-scalar diffraction relation [68]. Esmer made extensions to Delen's method for diffraction pattern calculation between arbitrarily oriented planes [57].

Basics of the angular spectrum method is well explained in [53] with different examples. The bases of the method is to represent signals in frequency domain and do the propagation, rotation and shift operations in this domain accordingly. More specifically, a wave at $z = 0$ plane denoted by $U_0(x_0, y_0, 0)$ can be represented in frequency domain as:

$$\begin{aligned} A(\nu_x, \nu_y, 0) &= \int_{-\infty}^{\infty} \int_{-\infty}^{\infty} U_0(x_0, y_0, 0) \exp[-j2\pi(\nu_x x + \nu_y y)] dx dy \\ &= \mathcal{F}\{U_0(x_0, y_0, 0)\}, \end{aligned} \quad (3.1)$$

where $\nu_x = \alpha/\lambda$, $\nu_y = \beta/\lambda$ are spatial frequencies and α , β are the directional cosines of the plane wave. The wave at another plane at a distance d is:

$$A(\nu_x, \nu_y, d) = A(\nu_x, \nu_y, 0) \exp\left[j2\pi d \sqrt{1/\lambda^2 - \nu_x^2 - \nu_y^2}\right]. \quad (3.2)$$

A good feature of the angular spectrum method is that rotations and shifts in the object plane or in the recording plane can be done easily by adding necessary kernel to the Eq. 3.2. This allows calculation of the object wave between arbitrarily oriented object and recording planes without adding any computational complexity to $2\mathcal{O}(N^2 \log N) + 2\mathcal{O}(N^2)$.

The methods described up to now are the exact calculations of the wave propagation. However, in general the distance between the object and the recording plane is much larger than the lateral dimensions of the object which calls utilization of Fresnel

transform. The importance of the Fresnel transform comes from its fast evaluation property. Computational complexity comes from calculation of the quadratic terms inside and outside the Fourier transform, element by element matrix multiplication and Fourier transform. Hence complexity of the method is $\mathcal{O}(N^2 \log_2 N) + 2\mathcal{O}(N^2)$. Present form of the Fresnel transform is applicable only to planar objects not for 3D objects. Here we propose the Planar Layers Method (PLM) which utilizes the fast nature of Fresnel transform to calculate the diffraction pattern of any 3D object. The method will be explained in the next section and compared with the PPM in terms of computational time and accuracy.

As it is previously stated Fresnel transform will give correct results at distances where Fresnel approximation holds. This limitation is surpassed by a method based on fractional Fourier transform [69] and it is generalized for a wide range of integrals in [70]. Like the Fourier transform and the fractional Fourier transform, a connection between wavelet transform and the wave propagation is established in the literature [47, 71, 72]. There are also methods that focus on specific cases. For example in [73] the wave equation is solved in cylindrical coordinates and the propagation of cylindrical, conical and helical waves are described. Furthermore Rosen considered the case of reconstructing a computer-generated hologram to a curved surface [74]. A different approach is derived by Matsushima for computer generated holograms of objects that has shade and texture [52].

3.1 Planar Layers Method (PLM)

The methods described up to now leads to a search for a method that is fast like the Fresnel transform and precise like pointwise calculation. The PLM we propose here utilizes the fast nature of the Fresnel transform and it is an approximation to

the pointwise propagation method. In the PLM we represent 3D objects by discrete planar layers -all perpendicular to the recording plane- where each layer has a depth value and a transparency such that when the layer transparencies are added up the result will be the 2D view of the object from the recording plane perspective. Hence any 3D object is represented by an intensity map and a depth map as shown in Fig. 3.1. For each distance value intensity values of the object are taken and the remaining parts of the layer is padded with zero up to the dimensions of the recording plane as shown in the lower part of the Fig. 3.1. Then it is possible to propagate each layer's field using Fresnel transform and since the wave propagation is a linear system, superposition of the fields should give the same result with the PPM.

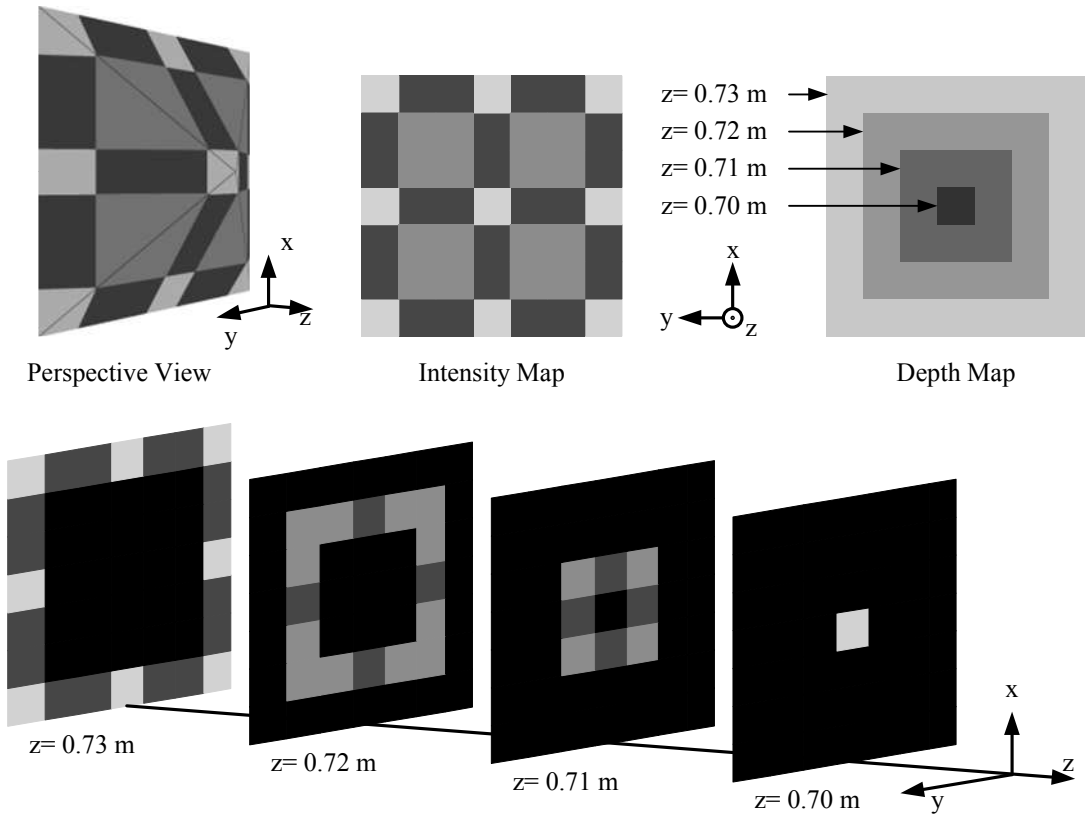


Figure 3.1: Perspective view of a simple pyramid. For this pyramid intensity map and depth map that is seen from z -axis is shown. In order to propagate using PLM, for each depth value ($z = 0.70, 0.71, 0.72, 0.73$) corresponding intensity values are taken from intensity map and the remaining parts are padded with zeros.

3.2 Numerical Results

A more complicated example is shown in Fig. 3.1 where a cube covered with USAF resolution chart is used as an object. The cube is rotated by 45° in both x and y axes in the counter clockwise direction and viewed from the $+z$ direction. For that perspective, intensity map and depth map is shown in the same figure. Depth map contains $M = 202$ unique distance values from nearest to farthest point of the cube hence we will have 202 layers to be propagated. Nearest point of the cube is at $d = 0.7m$ and farthest point is at $d = 0.7071m$. Dimensions of the cube are $5.9mm \times 5.9mm \times 5.9mm$. The recording plane is sampled by 512×512 with pixel dimension of $30\mu m$ by $30\mu m$. In Fig. 3.2 magnitudes of the object waves that are calculated using the PPM (U_{PPM}) and the PLM (U_{PLM}) are shown. There is no noticeable difference but proper error analysis is done by calculating the mean-squared-error (MSE) between U_{PPM} and U_{PLM} . MSE is calculated using:

$$MSE = \sum_{m=1}^N \sum_{n=1}^N \frac{(|U_{PLM}(m, n)| - |U_{PPM}(m, n)|)^2}{N^2} \quad (3.3)$$

The MSE mainly originates from the Fresnel approximation but it is 0.54% for the cube which is considerably small.

In complexity calculation of the PLM there are two main factors that has contribution: Fresnel transform and the quadratic phase terms. Therefore computational complexity of the PLM will be $M [2\mathcal{O}(N^2) + \mathcal{O}(N^2 \log N)]$ for an object represented by M layers over an $N \times N$ grid whereas it was $\mathcal{O}(N^4)$ for the PPM. If the number of object points is not N^2 , say N_o then the complexity calculation for the PPM must revised to $\mathcal{O}(N_o N^2)$. The simulation of the pyramid in Fig. 3.2 is done using Matlab software on a 3 GHz Xeon quadcore PC. Simulation using PPM takes around 139 hours, whereas it takes just 718 seconds with the PLM.

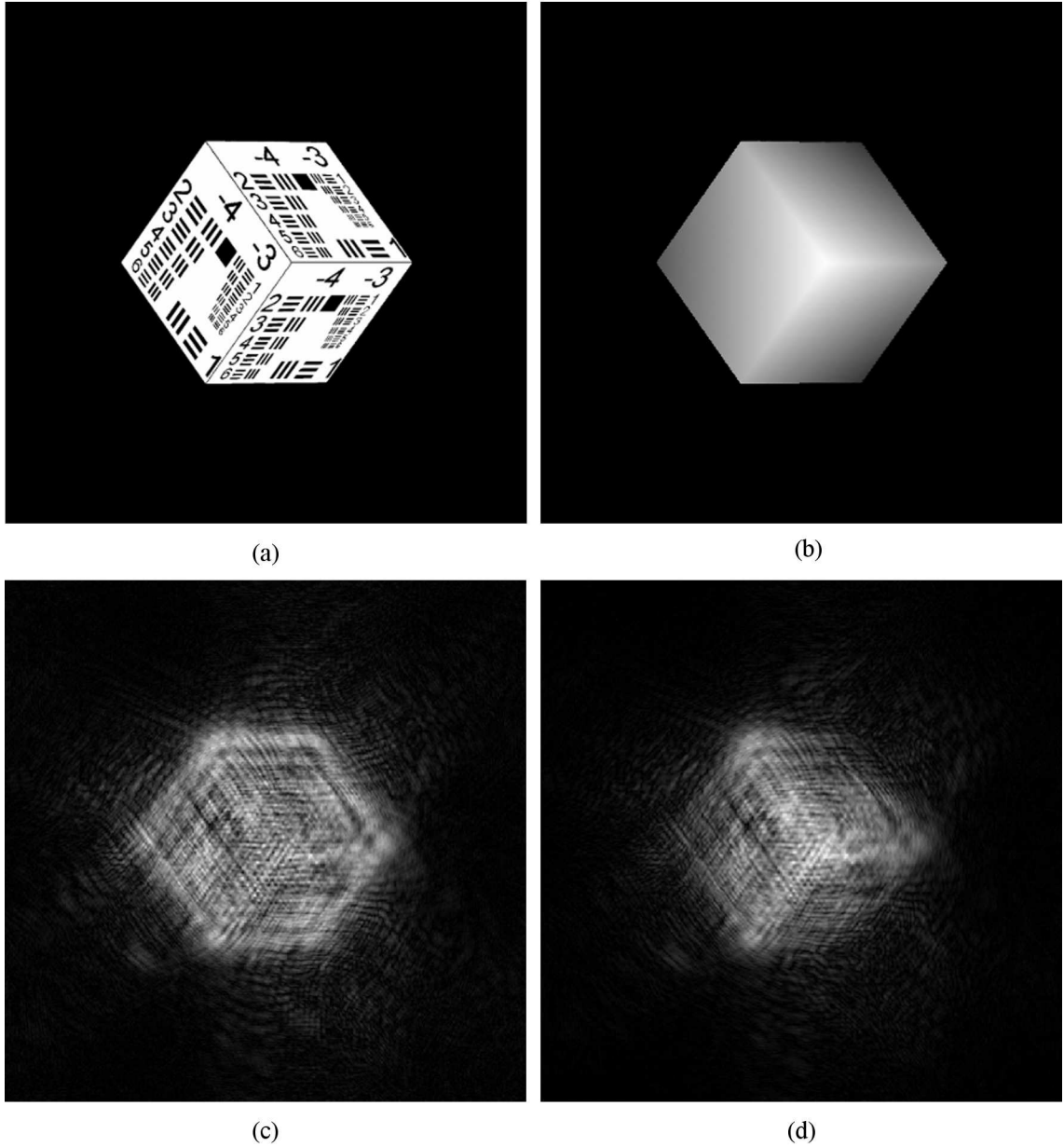


Figure 3.2: (a) A cube that is covered with USAF resolution chart with dimensions of $5.9\text{ mm} \times 5.9\text{ mm} \times 5.9\text{ mm}$. It is rotated by 45° in x and y axes. (b) Depth map for the cube. There are 202 unique depth values where nearest point is at $d = 0.7\text{ m}$ and farthest point is at $d = 0.7071\text{ m}$. (c) Object wave of the cube calculated using PPM. (d) Object wave that is calculated using PLM. Visually they are quite same but a more proper error analysis is done in the text.

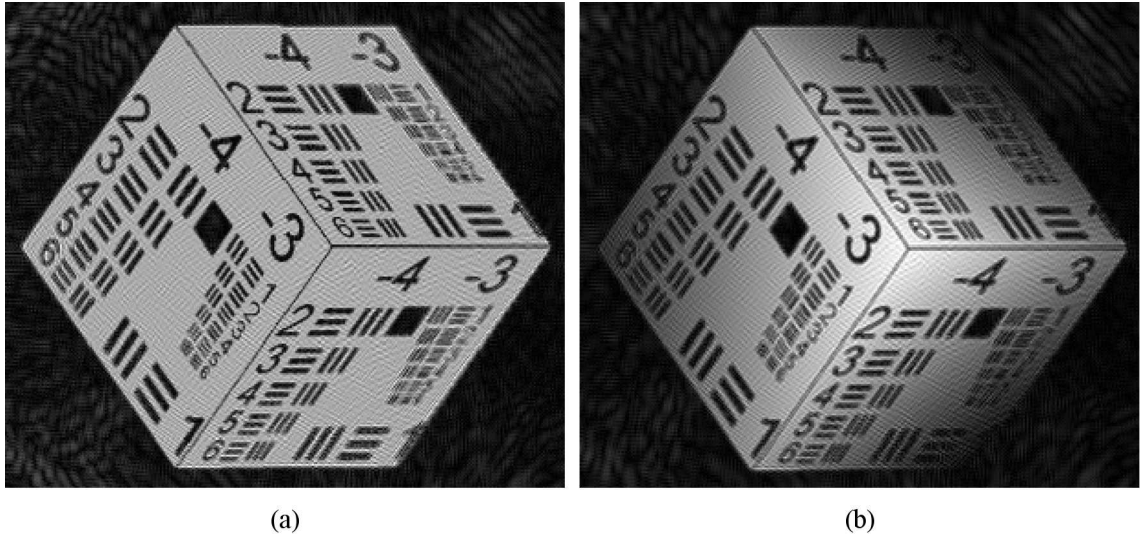


Figure 3.3: Reconstruction results at $d=0.7$ meter for the holograms generated by (a) PPM and (b) PLM

Here we give the reconstruction results for the holograms calculated using the PPM and the PLM. Holograms are formed by adding plane reference wave to each of the object waves with a slight angle to simulate the off-axis scenario. Zero-order noise is filtered using phase-shifting [19, 38] and holograms are reconstructed. The result is shown in Fig. 3.3 where only the real images are shown, conjugate images are cropped out.

The PLM is explained in detail for 3D imaging up to now. Apart from 3D imaging, holography can be used in interferometric testing applications such as surface deflection measurements and vibration analysis. In chapter 5 evaluation of the holograms of deflected or vibrating surfaces using the PLM will be given and simulation results will be compared with the experimental results.

4 HOLOGRAPHIC RECORDING WITHOUT A SEPARATE REFERENCE WAVE

In a generic holography setup we split the laser illumination into two arms and one is used to illuminate the object and the other one is used as the reference wave after expanding and collimating it. To record a high quality hologram we need to have a good interference. This can be achieved if the difference between the path lengths traveled by the object wave and the reference wave is within the coherence length of the laser. Hence pathlength equalization procedure is an important step in hologram recording. Here we present a method to simplify the pathlength equalization step that relies on creating a reference wave from the reflected object wave. Therefore we do not need to split the laser beam into two arms or a separate reference arm, i. e. we directly illuminate the object. Since reference wave is generated from the object wave itself, desired pathlength equalization of the object wave and the reference wave is done automatically. This makes possible to record holograms of objects at arbitrary distances with the same holography setup.

Reference wave in our setup is a plane wave hence if someone wants to create a plane reference wave from a distorted wavefront, s/he must filter the high frequency component on the wavefront and take only the DC component. In the literature there is some related work on this subject: For example in reference [75] an object beam is split into three different waves and the zero order is filtered with a pinhole. Afterwards first order waves are allowed to interfere with the filtered zero order term. However,

in their experiments there is already reference wave present in the object wave since they used an object in transmission mode which only partially covers the laser beam. One other reference [76] considers a holographic recording without a reference beam but here it is assumed that object have some arbitrary set of coherently luminous points. Also another reference [77] mentions local reference beam generation from the object wave using a pinhole filter however their experimental result is not clear since their object wave already contains reference wave as they used an aperture as the object in transmission holography. Finally in another reference [78], reference beam free recording of holograms are presented but this is a special case where object is placed "suitably close" to the hologram plate and it is irrelevant to our method presented here.

4.1 Experimental Setup

Spatial filtering is generally done using a pinhole system in an optical setup. We can not create a good plane reference wave using the pinhole system unless there is a notable DC reflection from the object. However our method uses a single mode optical fiber as the spatial filter. The waves coming to the optical fiber will couple in if its incidence angle is smaller than the numerical aperture of the fiber. In our method we use a single mode fiber hence the higher order modes die out and only the principal mode which is a perfect Gaussian beam propagates along the fiber and available at the exit. This Gaussian beam is then expanded and can be used as the plane reference wave.

The experimental setup for the method is shown in Fig. 4.1. This is a modified version of the Mach-Zehnder interferometer which uses two beam-splitters to divide and combine the wave. The object is illuminated directly with the expanded laser light and the light diffracted from the object is split into two with the first beam-

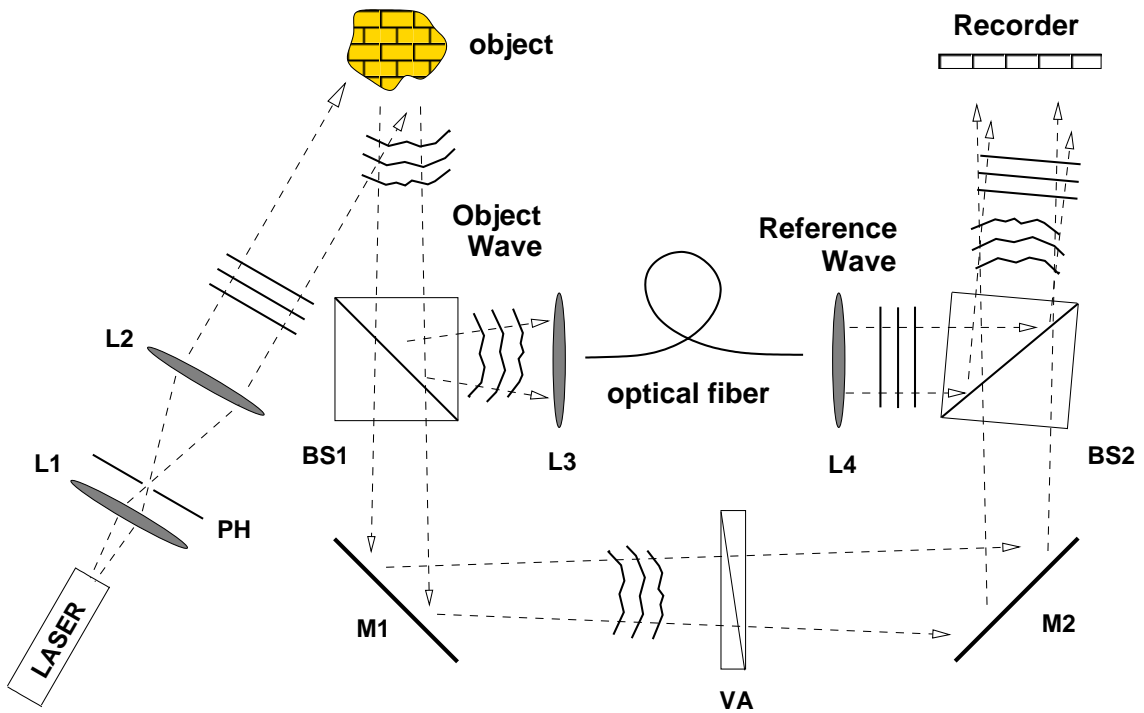


Figure 4.1: Setup for recording holograms without a separate reference wave. Lens 1 and Lens 2 and a pinhole (PH) is used for cleaning up and enlarging the laser beam. The object wave is split with a beamsplitter (BS1) and one of the beams is focused into a single mode fiber with a lens (L3). At the exit end of the fiber is the reference wave and it is converted to a plane wave with another lens (L4). The resultant reference wave is combined over a second beamsplitter (BS2)-rotated slightly for off-axis hologram recording- with the other part of the object beam routed around with two mirrors (M1 and M2). Two combined waves are allowed to interfere at the CCD and the interference intensity is recorded. Note that there is a variable attenuator (VA) in the path of the object beam after the first beam splitter in order to equalize powers in the reference wave and the object wave to maximize the interference pattern as it is explained in the text.

splitter. One of the arms is focused using a lens to a single mode fiber and the exiting light is collimated using another lens. This is a plane wave with Gaussian profile which can be used as the reference wave. This reference wave is interfered with the other half of the object wave at the second beam-splitter. The resulting interference pattern is recorded using a CCD camera which is our hologram. Pathlength equalization will be automatically satisfied if pathlengths between two beam-splitters are matched as it can be seen from figure.

4.2 Results

Using this experimental setup holograms are recorded without separate reference wave. In the setup a 30 mW HeNe laser is used as the light source. The object is illuminated with that light source after expanding it enough to cover the object. Two coins that one of them partially occludes the other is used as the object at a distance of 140 *cm* from the CCD. The diffracted object wave is split into two beams with a 35 *mm* cube beam splitter and one of the beams is focused with a lens ($f = 75 \text{ mm}$) to a single mode fiber (single mode at 632.8 *nm*). Fiber length was kept at 30 *cm* which was long enough to work comfortably with and it was long enough to let the higher order modes die out. Another lens with a focal length of $f = 75 \text{ mm}$ is used at the exit of the fiber to convert the point source like radiation to a plane reference wave. The power of the reference beam for this experiment measured approximately as 7 *nW*. The profile of the produced reference wave is shown in Fig. 4.2. It is a Gaussian distribution as expected. Even more when we take a cut from this profile, the result is as shown in Fig. 4.2 with blue. We can fit a Gaussian function to this distribution such as the one shown in red.

Since there is substantial power loss in the path through the single mode fiber power equalization between interfering waves is needed. Therefore a variable attenuator is used on the object beam path. The power ratio between the reference wave and the object wave in an interferometer is equal to unity to have the maximum fringe contrast, where as it is more than unity in holography. In holography rule thumb power ratio is generally equal to four in order to minimize the first order diffraction. Returning to the plane wave that we obtained after the collimating lens, this wave is used as the reference wave and it is combined with the other half of the object wave over a 35 *mm* cube beam splitter. The combined waves fall onto a CCD which

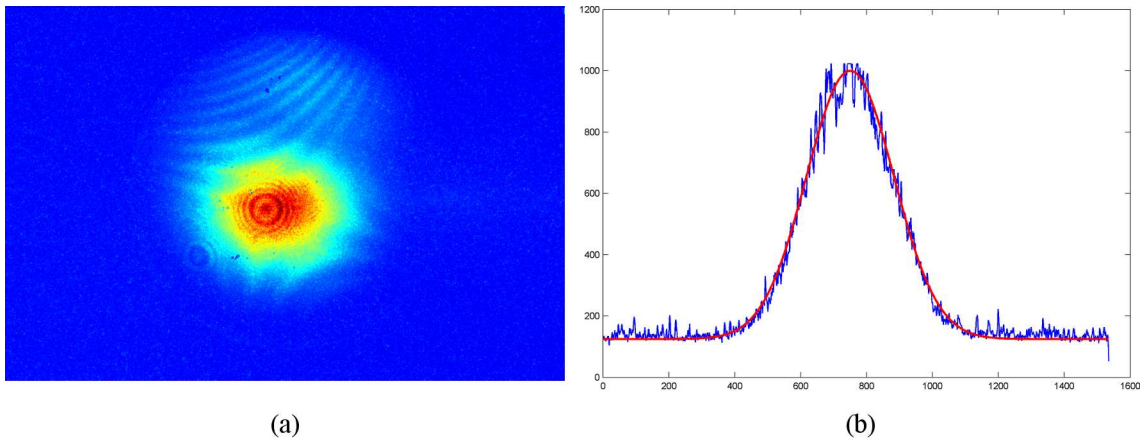


Figure 4.2: a) 1534×1024 pixels hologram of the two coins recorded in off-axis configuration with a 30 mW HeNe laser. The pixel dimensions of the CCD are $9 \mu m \times 9 \mu m$. b) Magnitude of the reconstructed hologram at a distance of $d = 140 \text{ cm}$. It is clearly seen that the hologram of two coins are reconstructed successfully, zero order and the conjugate image is also apparent. Note that the reconstructed image is also 1534×1024 pixels but the pixel dimensions are different so that its actual shape becomes a square. Since from the Fresnel diffraction theory the pixel dimensions in the reconstructed image is: $\lambda d / N_x \Delta_x = 45.8 \mu m$ and $\lambda d / N_y \Delta_y = 68.6 \mu m$ for the horizontal and vertical directions where $N_x = 1534$ and $N_y = 1024$ are the number of pixels in the horizontal and vertical directions, $\Delta_x = \Delta_y = 9 \mu m$ and d is the object to CCD distance.

had a (1534×1024) array of $9 \mu m \times 9 \mu m$ size pixels and the resultant interference intensity is recorded as the hologram. Fig. 4.3 shows the actual recorded hologram and numerically reconstructed magnitude of the hologram at a distance of 140 cm . It is clearly seen in this figure that the hologram is recorded and reconstructed successfully with this method. Once the pathlength equalization is done this holography setup can be used to capture the holograms of any object at arbitrary distances like a point-and-shoot holographic camera.

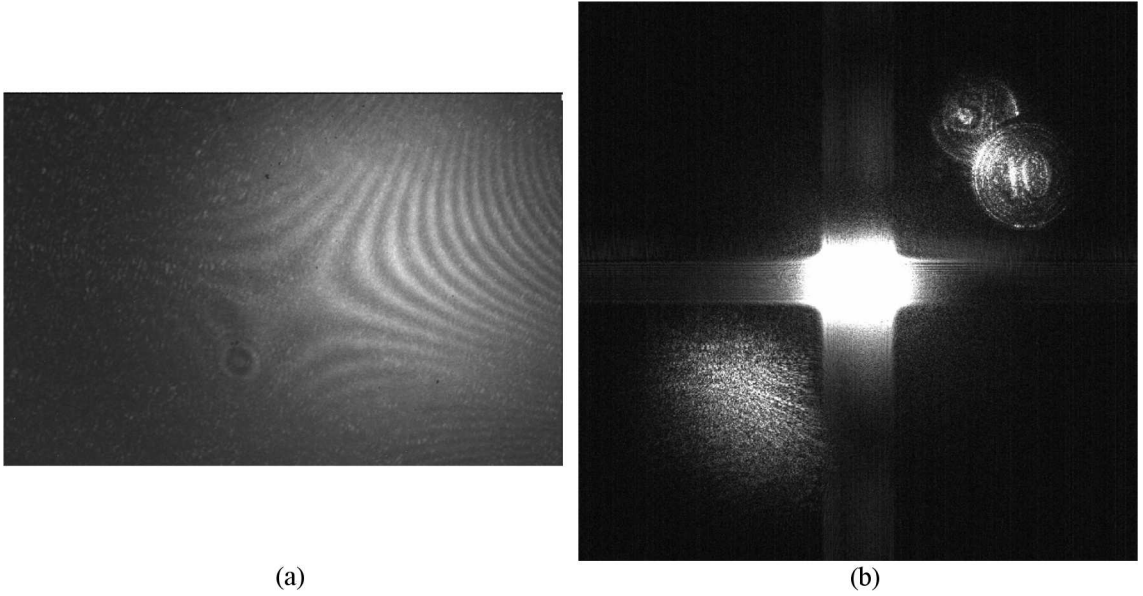


Figure 4.3: a) 1534×1024 pixels hologram of the two coins recorded in off-axis configuration with a 30 mW HeNe laser. The pixel dimensions of the CCD are $9 \mu m \times 9 \mu m$. b) Magnitude of the reconstructed hologram at a distance of $d = 140 \text{ cm}$. It is clearly seen that the hologram of two coins are reconstructed successfully, zero order and the conjugate image is also apparent. Note that the reconstructed image is also 1534×1024 pixels but the pixel dimensions are different so that its actual shape becomes a square. Since from the Fresnel diffraction theory the pixel dimensions in the reconstructed image is: $\lambda d/N_x \Delta_x = 45.8 \mu m$ and $\lambda d/N_y \Delta_y = 68.6 \mu m$ for the horizontal and vertical directions where $N_x = 1534$ and $N_y = 1024$ are the number of pixels in the horizontal and vertical directions, $\Delta_x = \Delta_y = 9 \mu m$ and d is the object to CCD distance.

5 HOLOGRAPHIC INTERFEROMETER AND MICROPHONE ARRAY SYSTEM FOR IMAGING AND ANALYSIS OF VIBRATING SURFACES

With the invention of laser, along with its 3D imaging applications interferometric testing feature of holography is utilized more. Surface deflection measurements and vibration analysis are carried out using holographic interferometry [8–10]. Without any contact to the surface precise analysis is possible. Hence it is preferred in situations where surface characteristic can be affected by contact measurement techniques. Also it should be noted that, with a single holographic capture a surface can be analyzed completely. This is an important advancement over pointwise measurement techniques such as measurement with accelerometers and ranging techniques.

In this chapter, holographic deflection measurement technique is explained first. Surface deflection simulations with the PLM and the experimental results are also presented. Later vibration analysis with holographic interferometry is explained and PLM method is revisited to simulate the vibrations. Using the holographic interferometer it is possible to detect and image vibration amplitudes on the order wavelength of the light that is used in recording. Lastly a commonly used principle - acoustic vibration analysis - is introduced. Acoustic vibration analysis is done using a microphone array, hence microphone array signal processing is explained briefly. Acoustic analysis is given here, because we think that it can be a complementary

technique to holographic testing in the analysis of vibrations with large amplitudes. A combination of the systems would give analysis capability in a broad vibration amplitude range which is a desired testing technique for companies. To our knowledge this type of hybrid system is not designed in the literature. This chapter ends with experimental results obtained using the hybrid system.

5.1 Holographic Deflection Measurement

Holographic deflection measurement basically relies on phase difference of the deflected and the undeflected states of a surface. Hence in general, two holograms of the surface is taken; one is before the deflection and one is after the deflection. Then difference of these two holograms is reconstructed. Lets now consider the mathematical explanation of the technique.

Assume a surface with initial phase $\phi_0(x, y)$ which is deflected and observed from the directions θ_e and θ_o with respect to surface normal as shown in Fig. 5.1. If the surface is deflected by a small magnitude of Δd , amplitude of the wave propagating from the surface will remain unchanged, however phase will change as follows:

$$U(x_0, y_0) = |U(x_0, y_0)| \exp \left\{ -j \left[\phi_0(x, y) + \frac{2\pi}{\lambda} \Delta d (\cos \theta_e + \cos \theta_o) \right] \right\}. \quad (5.1)$$

It is seen from equation (5.1) that object wave will have the same phase when:

$$\frac{2\pi}{\lambda} \Delta d (\cos \theta_e + \cos \theta_o) = 2\pi m, \quad (5.2)$$

where m is an integer. For most cases, surface is deflected and observed from the surface normal ($\cos \theta_e + \cos \theta_o \approx 2$) thus displacement magnitudes of $\Delta d = m\lambda/2$ will have the same phase with the undeflected surface. Therefore, when the difference of

deflected and undeflected surface holograms is reconstructed we will observe a fringe pattern with dark and bright regions. In this fringe pattern, dark regions will correspond to the areas where deflection magnitude is a multiple of $\lambda/2$.

5.1.1 Simulation Results

For a deflected surface with known deflection magnitude if someone want to know what will the holographic measurement result will look like, computer simulations will be very informative. At this point, from the PLM perspective there is no difference between a 3D object and a deflected surface. In order to simulate surface deflections using PLM, again it is needed to represent the deflected surface with planar layers and then calculate the hologram. As an example assume a circular surface with a radius of 2.5 cm which is clamped from its perimeter and perturbed from its center with a small deflection of $\Delta d = \lambda/2$ as shown in Figure 5.1.(a). Deflected surface is discretized into planar layers and padded with zeros as shown in the figure. Each layer with the intensity pattern shown in Figure 5.1.(c) is propagated, superposed and interfered with a reference wave that has 0.6° angle to each transversal axis and a hologram is recorded. From this hologram, the undeflected surface hologram is subtracted and the difference hologram is reconstructed. In order to increase visibility, the zero order term is filtered using phase shifting and the real image is cropped out. From the figure, we can see that clamped perimeter of the surface where there is no phase difference is dark in the reconstruction result as expected. There is a dark-bright-dark transition as we move from perimeter to center and center is dark as expected since the deflection magnitude at the center is a integer multiple of $\lambda/2$. Below the reconstruction result a cut from the center is shown.

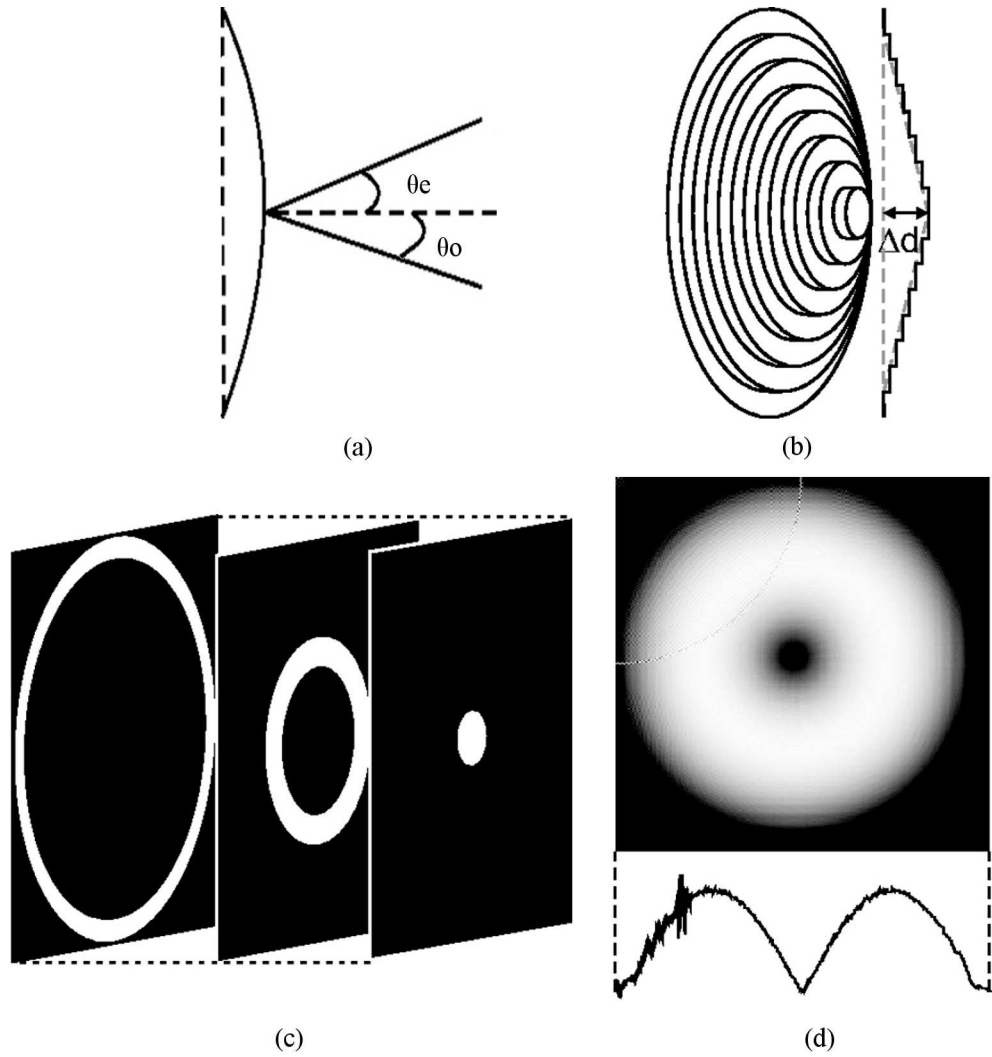


Figure 5.1: (a) A circular surface is deflected from its center to the direction θ_e and observed from direction θ_o . (b) Deflection magnitude of $\Delta d = \lambda/2$ is represented by 128 layer. In the figure only 8 layers are shown. (c) Layer by layer representation of the surface is shown with the intensity profiles of three layers. First layer has a circular intensity profile and rest of the layers have gradually increasing ring shaped intensity profiles. (d) There is one dark-bright-dark transition as explained in the text since the deflection magnitude is $\Delta d = \lambda/2$. A cut from the center is also shown and there are distortions on the left part due to real image term.

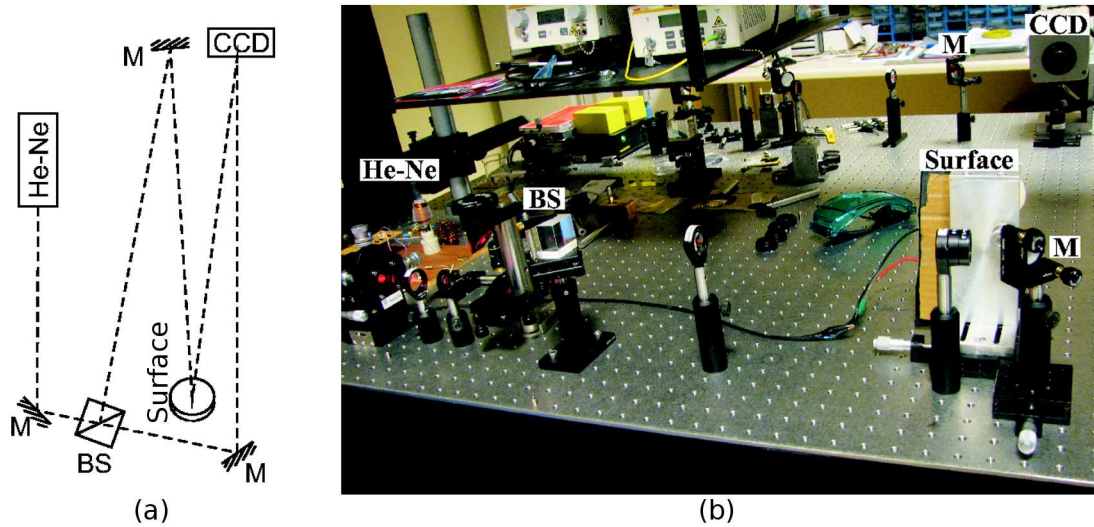


Figure 5.2: (a) Holographic deflection recording scheme, (c) Photograph of the experimental setup (He-Ne: Laser, M: Mirror, BS: Beam splitter, CCD: CCD Camera).

5.1.2 Experimental Results

For deflection measurement the holographic interferometry setup shown in Figure 5.2 is constructed. In this setup, an elastic surface with thickness $70 \mu m$ is stretched and glued to the front side of a circular loudspeaker with diameter of $58 mm$. A single polarized $30 mW$ He-Ne laser at wavelength $632.8 nm$ is used as the coherent light source and a MegaPlus 1.6i camera with 1534×1024 pixels with pixel dimensions of $9 \mu m \times 9 \mu m$ is used as the recording device. The distance between the surface and the camera is $0.7 m$ and the photograph of the overall experimental setup can be seen in Figure 5.2.

In the experiment, holograms of the surface at undeflected and deflected states are recorded. In first case, surface is deflected by $3 \mu m$, which is approximately equal to $\Delta d = 3 \mu m / 632.8 nm \approx 5\lambda$. Reconstructed image for this experiment is shown in Figure 5.3(a) where 10 fringes can be counted from perimeter to the center meaning that the deflection amplitude is 5λ . When same deflection is simulated with the PLM,

we get the result as in Figure 5.3(b). From this figure again 10 fringes can be seen as in the experimental result. Another experimental result for a deflection of $5 \mu m \approx 8\lambda$ is seen in Figure 5.3(c) and corresponding simulation result in Figure 5.3(d).

5.2 Holographic Vibration Analysis

The methods developed for holographic vibration analysis [8] at early stages were advanced by electronic reconstruction of the holograms and displaying them with a TV set [9, 79–83]. These tools are replaced by CCD cameras and computers after the rapid development in digital electronics technology [84]. Apart from difference in technology, there are different methods offered depending on the amplitude [85] and exposure type [84]. One of the methods among them is double-exposure time-averaged holographic interferometry where the exposure time is much longer than the vibration period. In this method two holograms of the surface is recorded, one of them while surface is stationary and one is while the surface is vibrating. At the last step difference of these two holograms is taken and reconstructed [9]. Now lets explain the mathematical formulation of the holographic vibration recording.

For the double-exposure time-averaged holographic interferometry assuming a surface is vibrating with frequency f , the object wave profile reflected from the surface will be:

$$U_0(x_0, y_0, t) = a_0(x_0, y_0) \cos(2\pi ft + \phi_0(x_0, y_0)), \quad (5.3)$$

where $a_0(x_0, y_0)$ is the amplitude and $\phi_0(x_0, y_0)$ is the initial phase distribution of the surface displacement. If a hologram of the surface is recorded, then the reconstructed image intensity $I(x, y)$ is proportional to [9]:

$$I(x, y) \propto I_0(x_0, y_0) J_0^2 \left[\left(\frac{2\pi}{\lambda} \right) a_0(x_0, y_0) (\cos \theta_e + \cos \theta_o) \right], \quad (5.4)$$

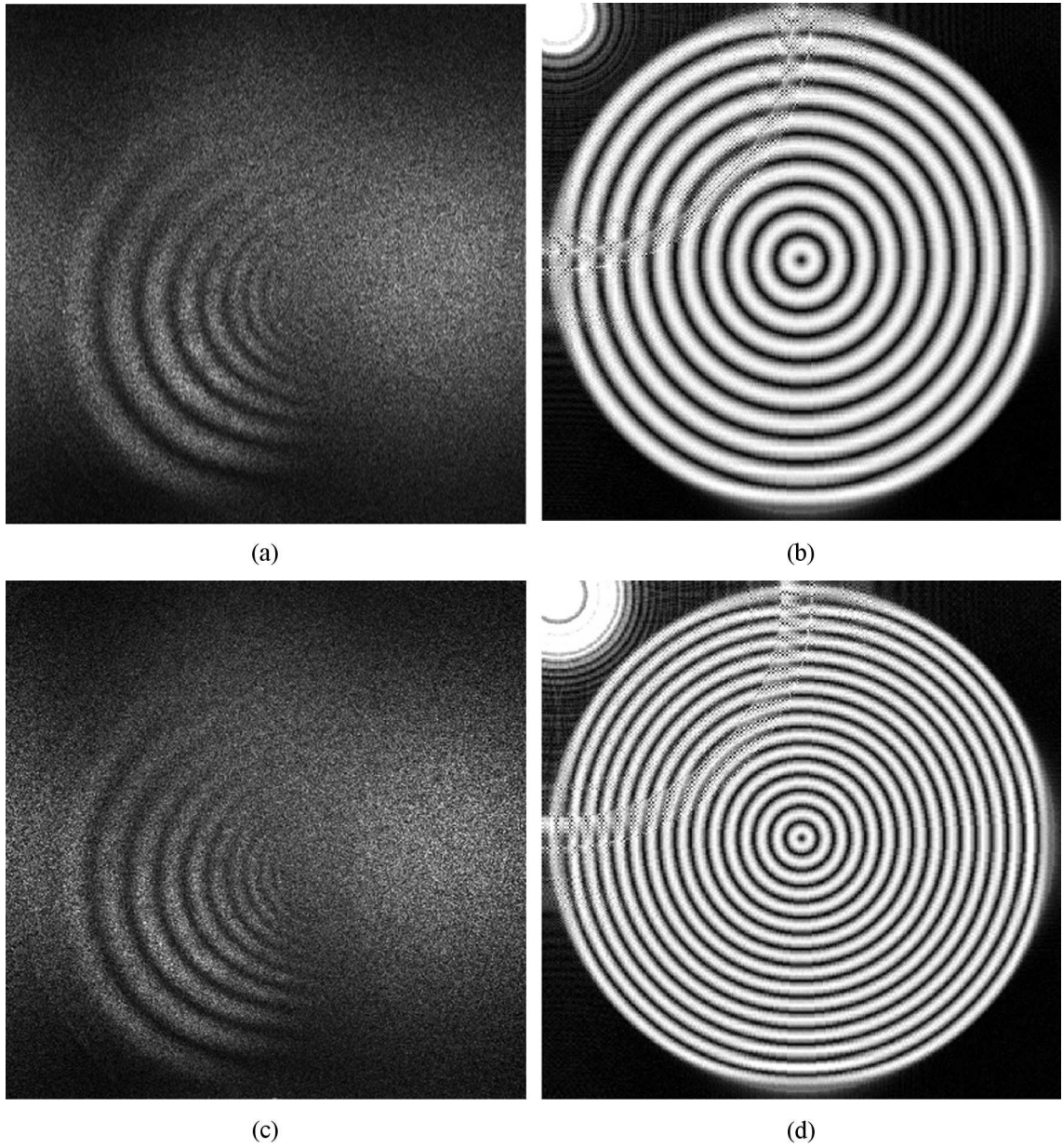


Figure 5.3: (a) Experimental result and (b) simulation result for deflection magnitude of $3\mu\text{m} \approx 5\lambda$; there are 10 fringes from perimeter to center. (c) Experimental result and (d) simulation result for deflection magnitude $5\mu\text{m} \approx 8\lambda$; there are 16 fringes from perimeter to center.

where $I_0(x_0, y_0) = |U_0(x_0, y_0)|^2$ is the surface intensity at rest and J_0 is the Bessel function of first kind at zeroth order [83]. Generally, angles between vibration direction and observation direction is small ($\cos \theta_e + \cos \theta_o \approx 2$) hence the surface intensity is modulated mainly with Bessel function. Therefore when the difference of the vibrating surface hologram and the non-vibrating surface hologram is taken, nodal lines of the surface will be brighter than rest of the image since nodal lines have no displacement and they correspond to $J_0^2(0)$. As the vibration amplitude increases the reconstructed hologram intensity will start to have fringes. Brighter parts will correspond to the local maximums of J_0^2 (which corresponds to vibration amplitudes of $3.8\lambda/4\pi$, $7.0\lambda/4\pi$, $10.2\lambda/4\pi$, $13.3\lambda/4\pi$, so and so forth) and dark regions will correspond to the local minimums of J_0^2 . Then if we know the region that correspond to J_0^2 , we can find the amplitude of the vibration by counting the fringes. Even if we do not know the regions for J_0^2 , holographic analysis will have much information. From any holographic reconstruction result we can determine the regions with large vibration amplitudes compared to the region with small vibration amplitudes. The regions with large vibration amplitudes will have narrow fringe spacing where as regions with small vibration amplitudes will have wider fringe spacing.

5.2.1 Simulation Results

Simulation of a vibrating surface can also be done using the PLM with properly handling the situation. If a surface is vibrating at its resonance frequency then it will have a steady mode shape. Hence knowing the vibration amplitude and mode number, we can calculate the holographic vibration analysis result. To do so for a given mode number, amplitude of the vibration is modulated with the Bessel function as in Eq. 5.4. Then simply we can use the result as the 3D input object for the PLM. As in

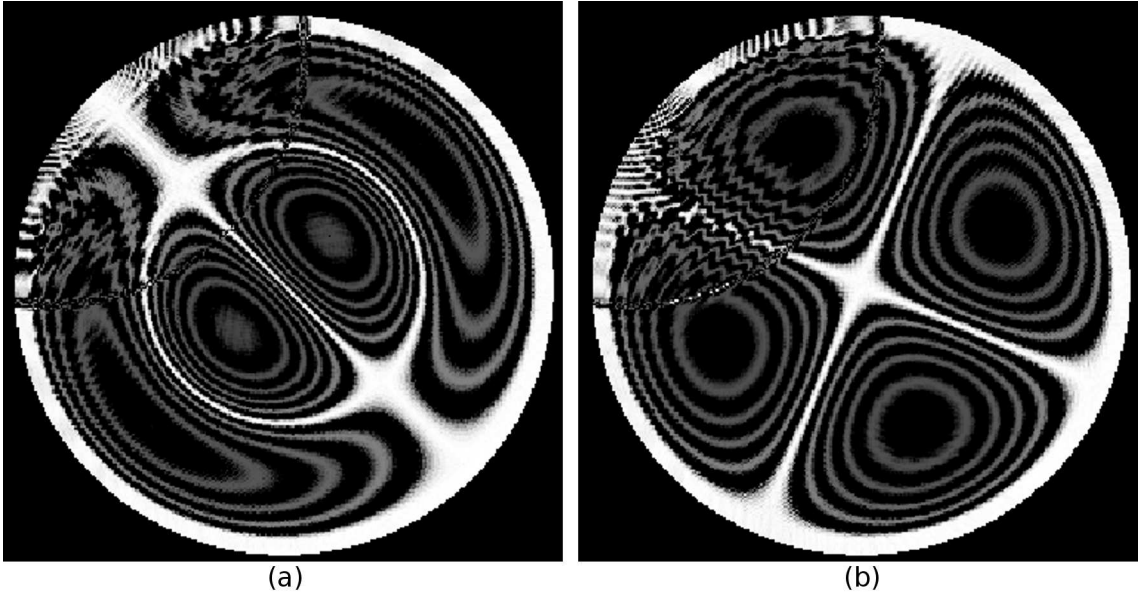


Figure 5.4: Holograms of the vibrating surfaces are recorded with PLM method for resonant mode (a) u_{12} and (b) u_{21} . Nodal lines are bright and as vibration amplitude increases fringing occur due to the behavior of the Bessel function.

the previous examples, discretization, zero-padding, propagation and then hologram recording steps are followed.

Simulations for the vibration analysis are done for the same circular surface as in deflection measurement. Two different resonant modes of the surface is simulated:

- 1) u_{12} mode in which rotationally there is one zero crossing and radially there are two zero crossings,
- 2) u_{21} mode in which rotationally there are two zero crossings and radially there is one zero crossing.

It can be seen from the simulation results in Figure 5.4 that the intensity is bright on the perimeter and at the nodal lines where vibration amplitude is zero. As we move from perimeter or a nodal line to areas of higher vibration amplitude, fringing occurs in accordance with the Bessel function.

5.2.2 Experimental Results

Vibration experiments are performed with the loudspeaker setup that was previously used in deflection experiments. The loudspeaker has resistance of 4Ω and it is driven over a series 47Ω resistor with a sine wave of amplitude 100 mV at two different resonant frequencies - 647 Hz and 1290 Hz -and two holograms of the surface are captured with an exposure time of 150 ms . Figure 5.5 shows the reconstructed difference of two exposures. From the results it is seen that the surface over the loudspeaker is not symmetric rotationally or radially (the tension of the membrane is not quite uniform). Hence fringe profiles obtained in the experiments are not exactly same with the simulations. However intensity is high at perimeter and at nodal lines as expected. Also fringing can be seen as we move away from perimeter and nodal lines. If we compare the result in 647 Hz and 1290 Hz we can conclude that we have higher vibration amplitude in 647 Hz since we have narrower fringe spacing.

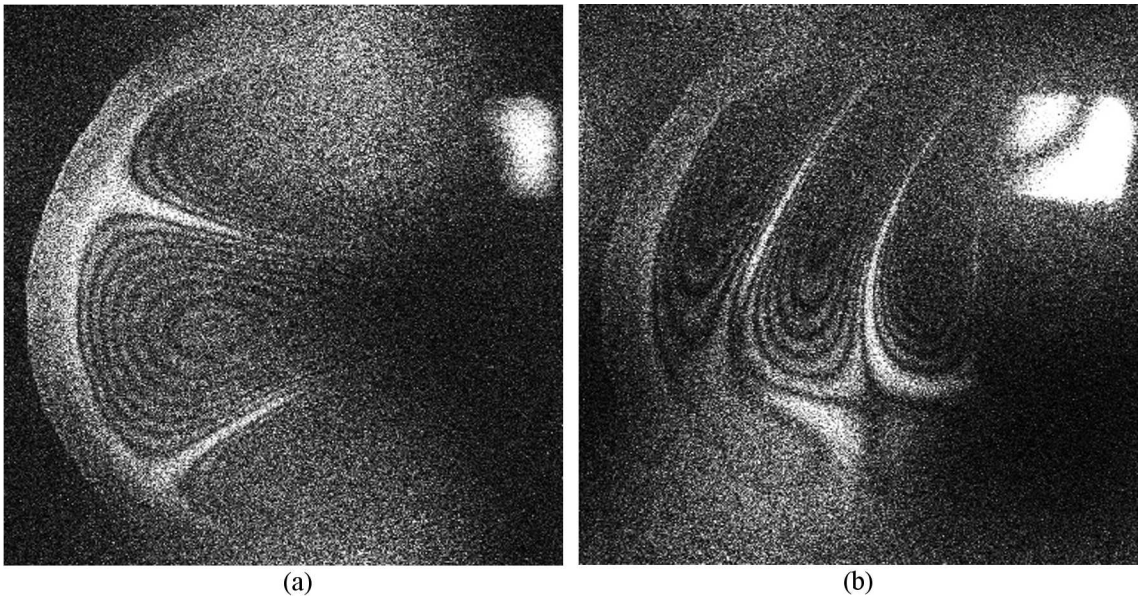


Figure 5.5: The loudspeaker (the same loudspeaker setup as in the deflection measurements) has resistance of 4Ω and it is driven over a series 47Ω resistor with a sine wave of amplitude 100 mV at two different resonant frequencies (a) 647 Hz and (b) 1290 Hz . Since the surface over the loudspeaker is not exactly rotationally or radially symmetric resulting fringes are not radially or rotationally symmetric.

5.3 Acoustic Vibration Analysis

In the previous section we have seen that vibration modes of a surface can be captured with a holographic interferometry system. Microphone arrays are other commonly used tools in vibration analysis. Hence here we briefly explain the principles of microphone arrays and signal processing in microphone arrays [86,87].

A microphone array stands for a set of microphones positioned in a specific orientation to collect sound data from the environment. They are used for teleconferencing, multi-party communications, robotic hearing, high-quality audio recordings, acoustic scene analysis, hearing aids and testing applications with ever increasing application areas. In the microphone array signal processing, first direction of arrival (DOA) or time difference of arrival (TDOA) is found to localize sound sources. From the reverse perspective DOA or TDOA corresponds to maximizing the main lobe of the directivity pattern of the microphone array in the sound source direction hence this is also called beamforming. Beam forming is done in a two step process: In the first step called synchronization, wavefronts of the arriving signals is equalized that results steering of the beam in different angles. In the next step called weight-and-sum, beam width of the main lobe, characteristics of the side lobes and nulls are determined. Important step in the beam forming is the selection of weighting coefficients. Coefficients can be selected before measurement or they can be adapted during the measurement to track a sound source. We conclude our review on microphone arrays here to keep it brief but a vast of literature is available on the topic [86], especially noting Benesty, Chen and Huang's book [87].

The acoustic system in this thesis is not developed from scratch but a commercially available product of *Head Acoustics*[©] is used. The system has both hardware

and software components. Hardware of the system composes of a microphone array and a module for recording, amplification and analog to digital conversion. Microphone array is formed with four high sensitive microphones (*HeadAcousticsMV210*)[©]. Here it is important to make the distinction between our system and a generic microphone array processing system. We used the microphone array just to get a rough estimate of the vibration (hence the noise) map over a single plane; we did not use it to generate the noise map on the planes at different distances. So we kept the microphone array as close as possible to the surface and generated the noise pressure map at the plane of microphone array. *Squadriga*[©] is the module that is used for recording, amplifying and sampling the sounds collected by the microphones. These components and a typical microphone array recording system is shown in Fig. 5.6. In the software side, *Artemis*[©] is used for exporting sound data from *Squadriga*[©] to computer and analyzing it. *Artemis*[©] has different signal processing features such as frequency spectrum analysis, filtering, resampling, power spectral density analysis and pressure map generation. In our application we need noise distribution over a surface hence pressure map generation capability was more important for us. For demonstration of the acoustic analysis, pressure maps of two objects are generated: A car door and an aluminum plate.

5.3.1 Car Door Experiment

Acoustics vibration analysis systems are commonly used in testing of automobile components. For example engines or doors of cars are tested using acoustic systems. In this experiment an interior structure of a car door (Fig. 5.7) is viewed with the microphone array system while its window motor is working. We have four microphones but it is possible to simulate a larger microphone array using these microphones. In

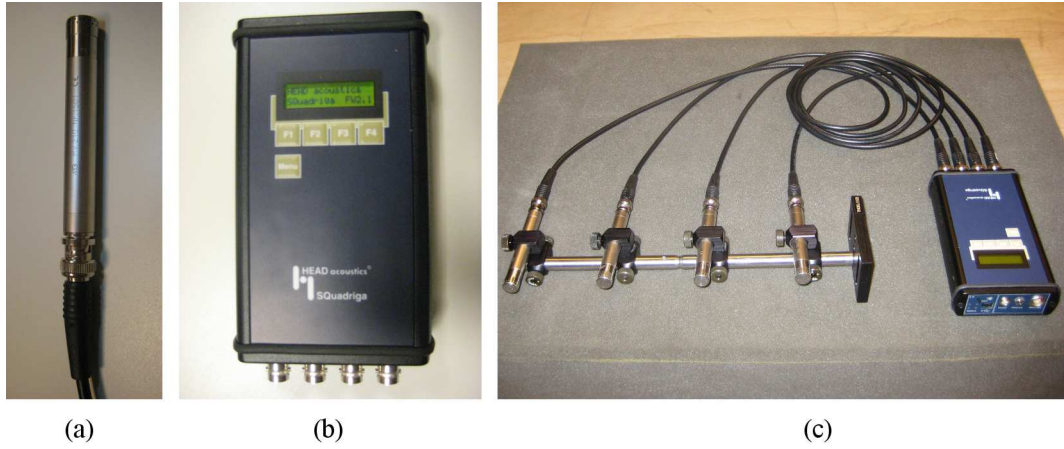


Figure 5.6: (a) Head Acoustics MV210 microphone (b) Recording and amplification module Squadriga (c) A typical linear microphone array for noise recording.

our experiment we formed a (1×4) horizontal microphone array and then shifted this microphone array up 8 times in the vertical direction in order to simulate an array of (8×4) . The spacing between two consecutive microphones was 6.4 cm and 3.2 cm in the horizontal and the vertical directions respectively as it is shown in Fig. 5.7. Hence an area of $(7 \cdot 3.2 = 22.4 \text{ cm} \times 3 \cdot 6.4 = 19.2 \text{ cm})$ is analyzed. This figure reveals that the areas with higher vibration amplitudes are mainly located around the motor. Also as the driving voltage increases pressure amplitude increases.

5.3.2 Aluminum Plate Experiment

In this experiment, an aluminum plate with thickness of 2 mm is stimulated. To do so a small magnet is glued at the center of this aluminum plate and it is pulled and pushed with an electromagnet coil. Electromagnet was made up of a coil with 900 number of turns wound on a steel core which has approximately $L \approx 6 \text{ mH}$ inductance. The electromagnet is driven by a wideband power amplifier which has a low output impedance. The power amplifier can deliver 50 W of power on a 4Ω load in the range $1 \text{ Hz} - 20 \text{ kHz}$. The aluminum plate - electromagnet setup and the power

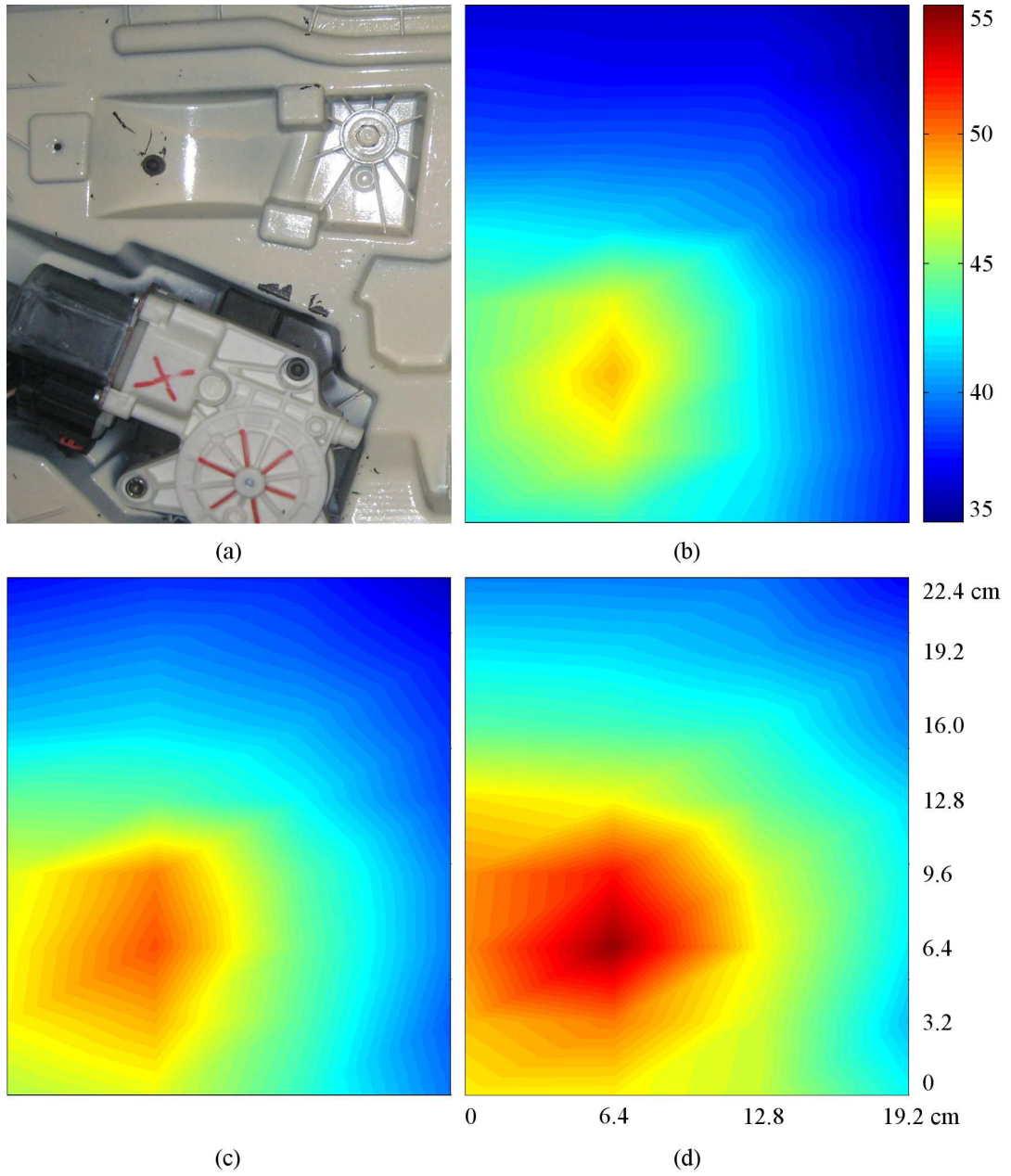


Figure 5.7: (a) A car door and pressure maps over a $(22.4\text{ cm} \times 19.2\text{ cm})$ area while its window motor is working at different driving voltages. (b) 10 V, (c) 15 V and (d) 20 V. As the driving voltage increases pressure amplitude increases.

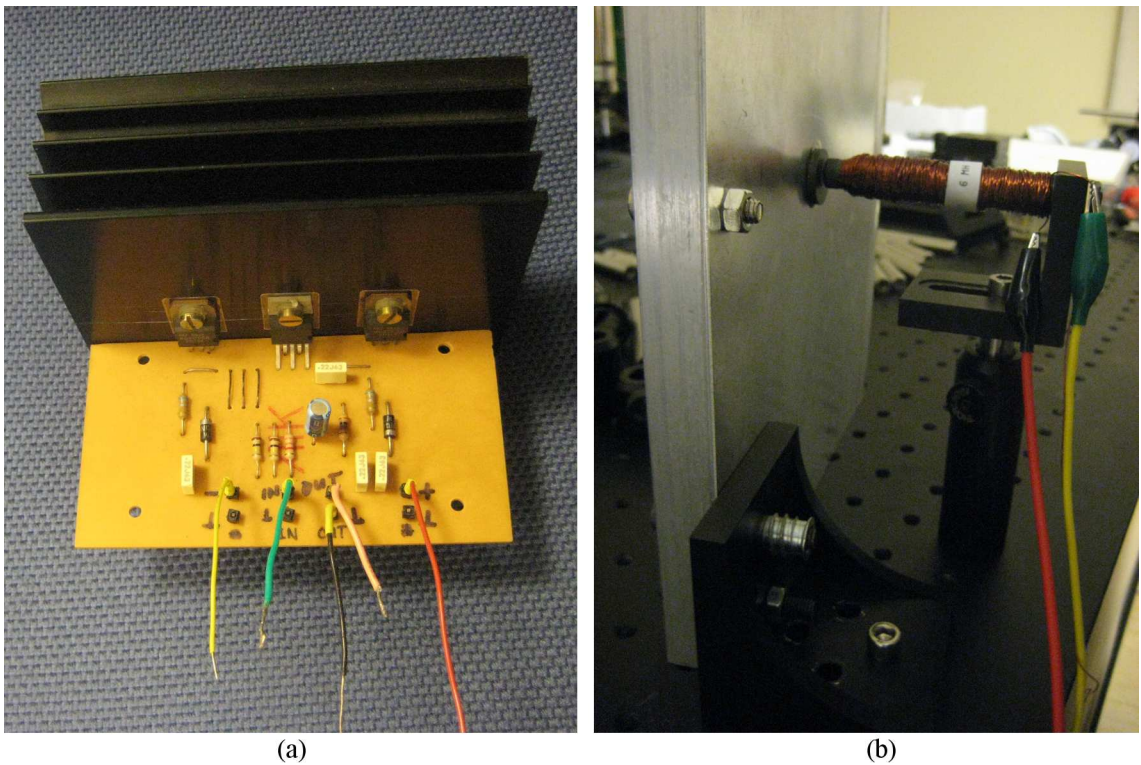
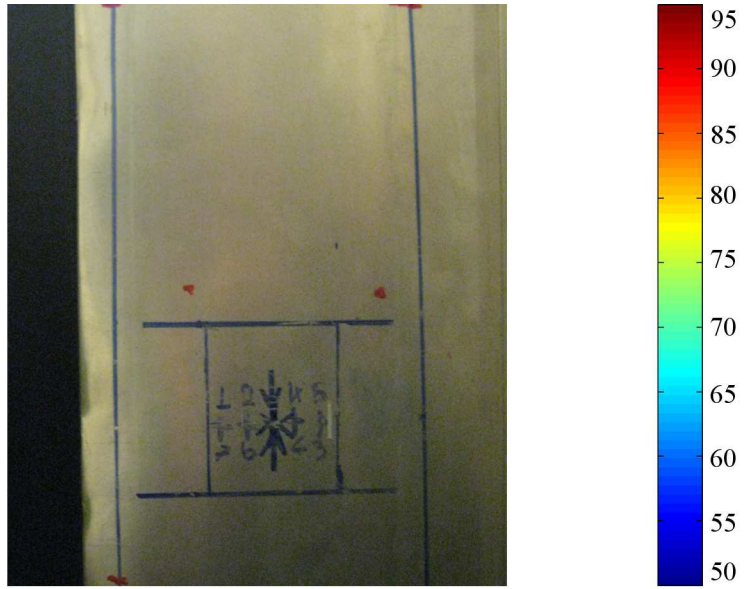
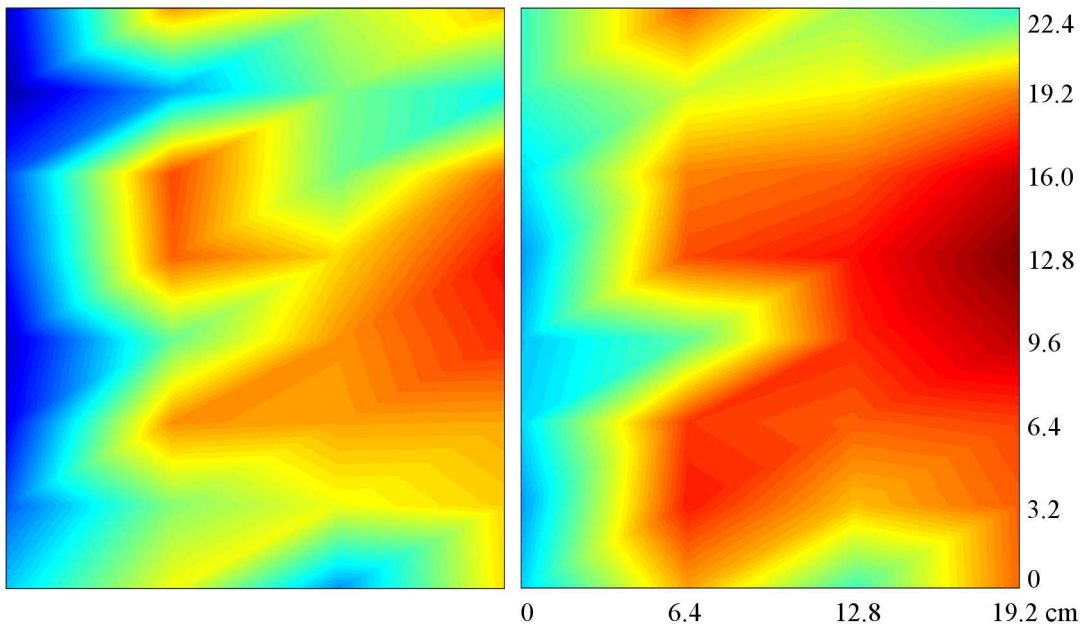


Figure 5.8: (a) Power amplifier. (b) Aluminum plate and the electromagnet setup.

amplifier is shown in Fig. 5.8. Using this power amplifier, electromagnet is driven with a sine wave at 570 Hz at two different amplitudes of $15 V_{pp}$ and $30 V_{pp}$. As in the previous experiment a microphone array matrix of (8×4) is simulated and an area of $(22.4\text{ cm} \times 19.2\text{ cm})$ is analyzed. The pressure map of the object is shown in Fig. 5.9. In Fig. 5.7 pressure contributions of all frequency components were summed up where as in this figure only the pressure map of the frequency component at the driving frequency is shown. As in the previous experiment we can determine the areas of high vibration amplitude and the increase in the maximum pressure as driving voltage increases.



(a)



(b)

(c)

Figure 5.9: (a) Aluminum plate and pressure maps of it over a $(22.4\text{ cm} \times 19.2\text{ cm})$ area when the electromagnet is driven by (b) 15 V and (c) 30 V .

5.4 Experiments with the Hybrid Opto-Acoustic Imaging System

Up to now we see that we can analyze vibrating object holographically and acoustically. To do a complete analysis the holography setup and the acoustic microphone array setups are incorporated as shown in Fig 5.10. Using the system first holographic and then acoustic recordings of the car door and the aluminum plate are done. Then holographic reconstruction result and the acoustic pressure map are compared.

5.4.1 Car Door Experiment

Car door is illuminated with the laser light at wavelength 632.8 nm and recorded with a camera that has 1534×1024 pixels in x and y axes respectively with pixel dimensions $9\ \mu\text{m} \times 9\ \mu\text{m}$. The car door motor was driven at three different voltages of 10 V , 15 V and 20 V . It is placed at distance 0.9 m , then using Eq. 2.5 the size of the area ($L_x = \lambda d / \Delta x \times L_y = \lambda d / \Delta y$) that will be analyzed using the holography setup will be $6.33\text{ cm} \times 6.33\text{ cm}$. Therefore a closeup analysis should be done using the acoustic system. Again a (8×4) microphone array is used but in order to increase the resolution, distance between microphones are decreased to 3.2 cm and 1.6 cm in horizontal and vertical directions respectively. Then the area that is analyzed using the acoustic system will have the dimensions of $11.\text{ cm} \times 9.6\text{ cm}$. In Fig 5.11 picture of the car door motor and its holographic analysis results at three driving voltages are shown. Fringe spacing decreases as the voltage increases. In the acoustic analysis (20 V) shown in Fig 5.12 there is a high pressure around the motor indicating the higher vibration. If we compare Fig 5.11 and Fig 5.12 we can conclude that at the areas of high vibration pressure fringes are steep and pressure map has a high magnitude.

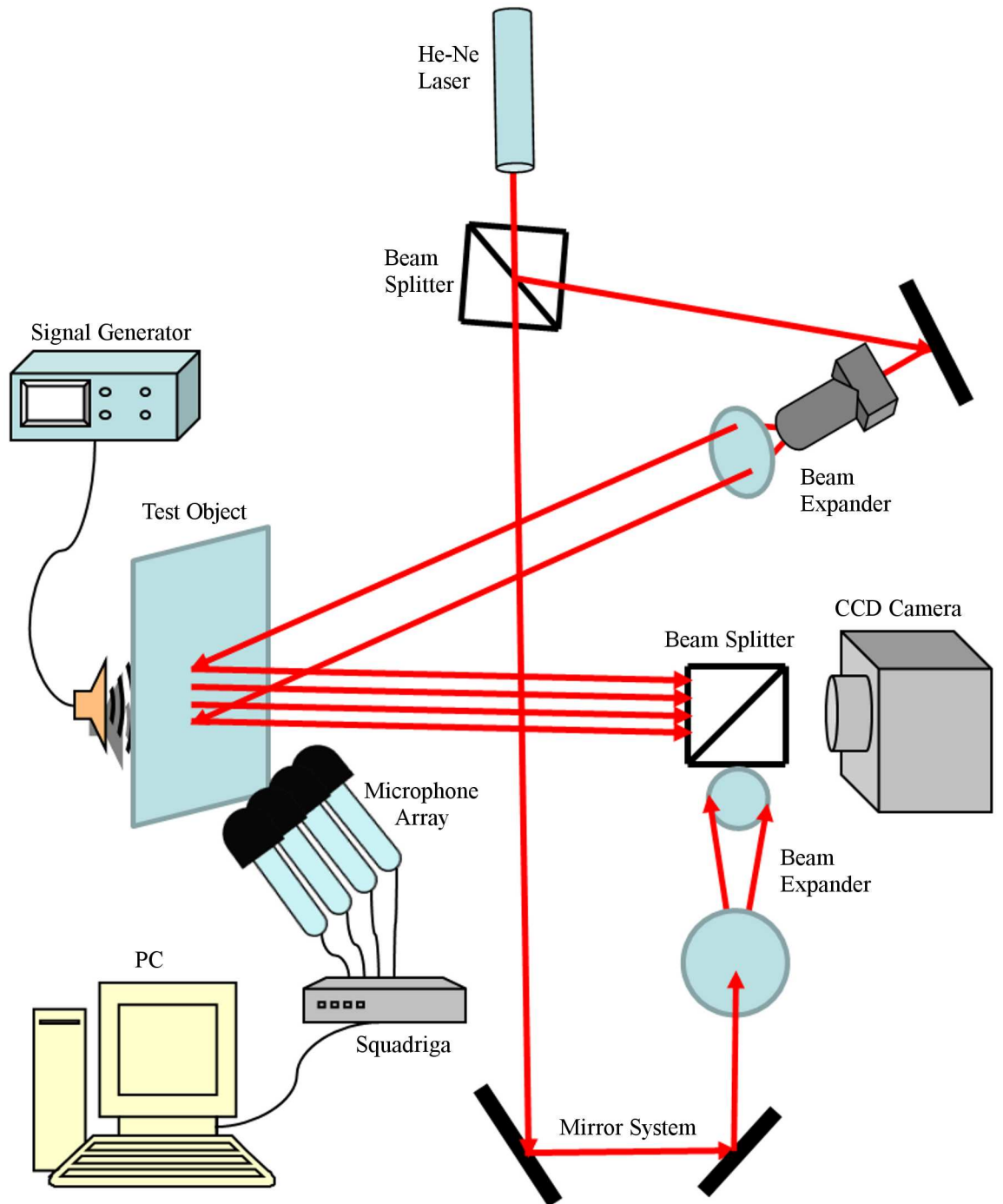


Figure 5.10: Hybrid opto-acoustic analysis system that is a combination of a holographic interferometer and a microphone array system.

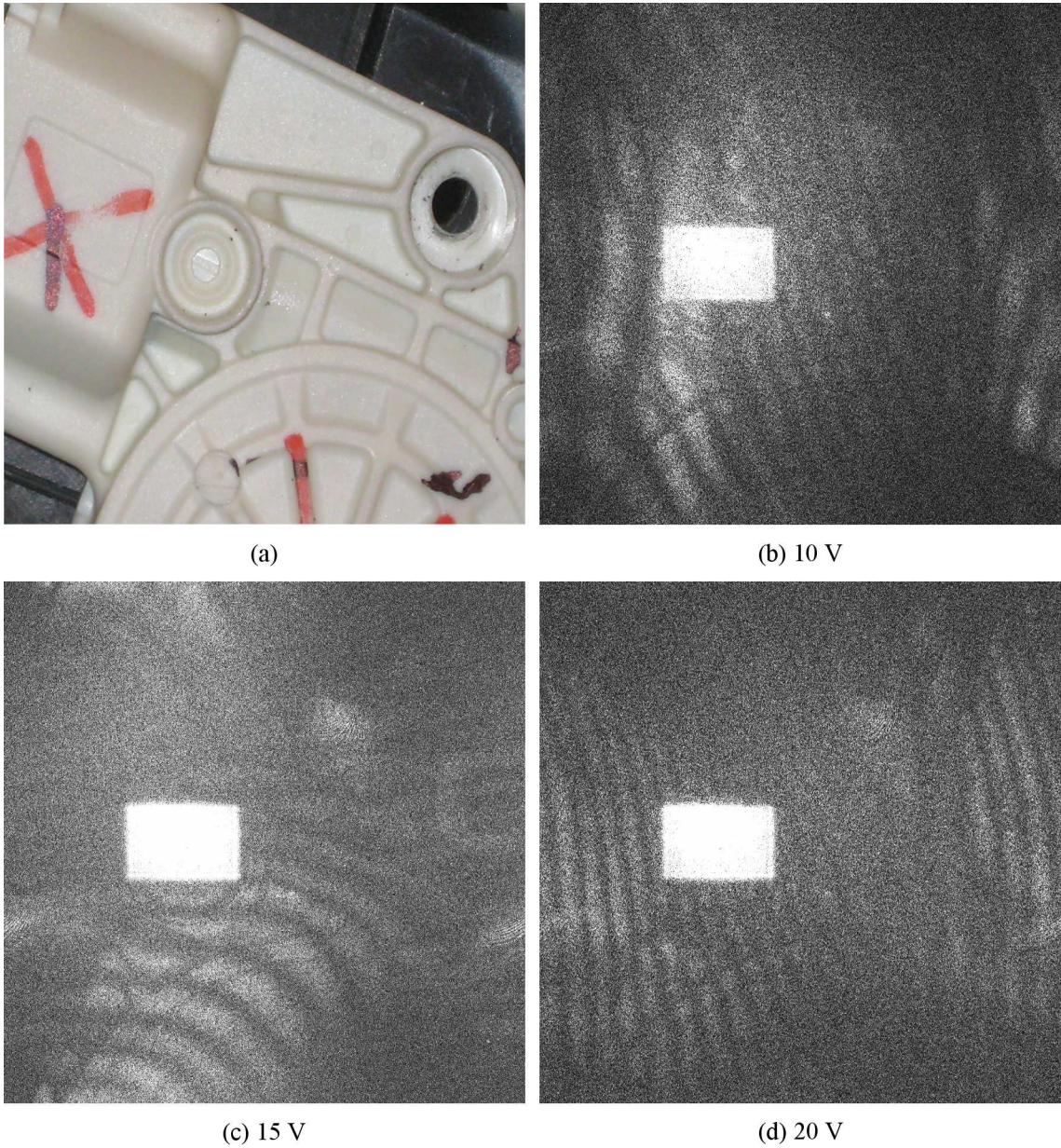


Figure 5.11: Vibration characteristic of the car door motor at three different driving voltages. The area imaged by the holographic system is $(6.33\text{ cm} \times 6.33\text{ cm})$ as explained in the text. Fringe spacing becomes narrower as the driving voltage is increased (a) 10 V , (b) 15 V and (c) 20 V . The fringes are especially focused at the left side.

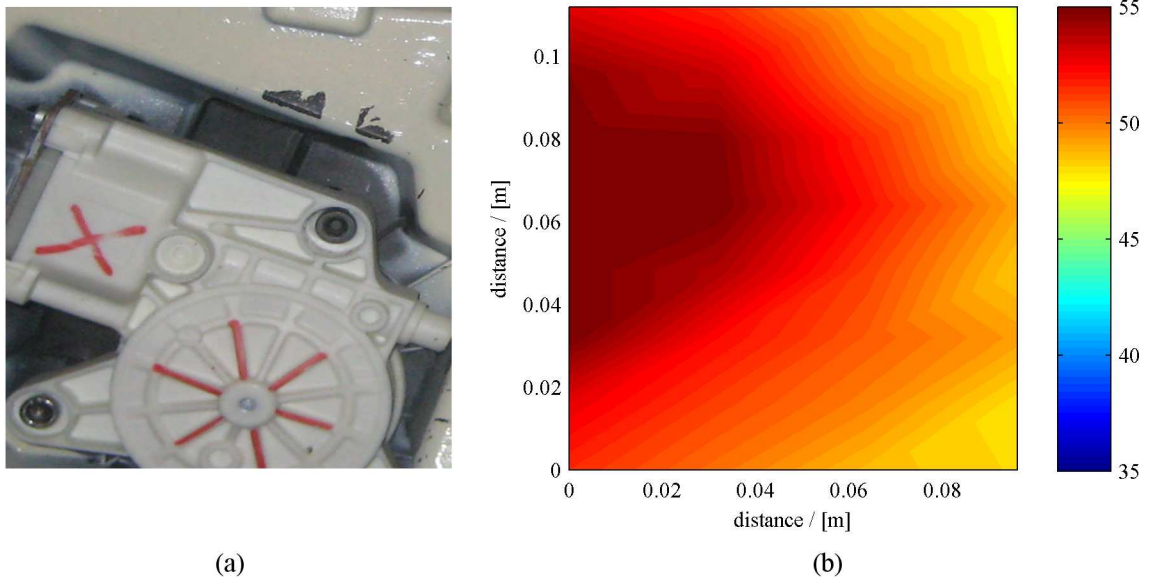


Figure 5.12: The same car door analyzed using the acoustics system when its window motor is driven by 20 V . The imaged area is $(11.2\text{ cm} \times 9.6\text{ cm})$. As in the holographic analysis vibration is mainly concentrated on the left side.

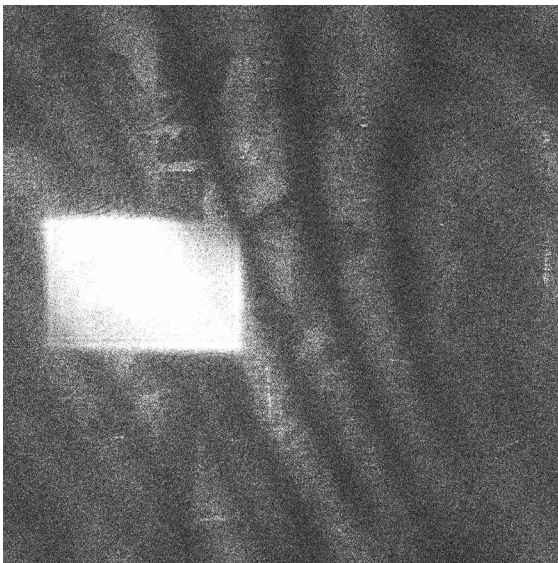
5.4.2 Aluminum Plate Experiment

This time aluminum plate is driven by 570 Hz signal with amplitude of 15 V and 30 V . It is placed 0.55 m far from the CCD hence the area that is imaged using the holography system has size of $3.87\text{ cm} \times 3.87\text{ cm}$. For the acoustics analysis the same orientation in the car door experiment is used for this experiment too, i.e. spacing of the microphones and the covered area is the same, $11.\text{ cm} \times 9.6\text{ cm}$. In Fig 5.13 close view of the analyzed area and its holographic analysis results at two different driving voltages are shown. Fringe spacing decreases as the voltage increases. In Fig 5.14 acoustics analysis result with the surface picture is shown. Comparing Fig 5.13 and Fig 5.14 it can be said that in the areas of high vibration pressure fringes become steeper and pressure map has higher magnitude.

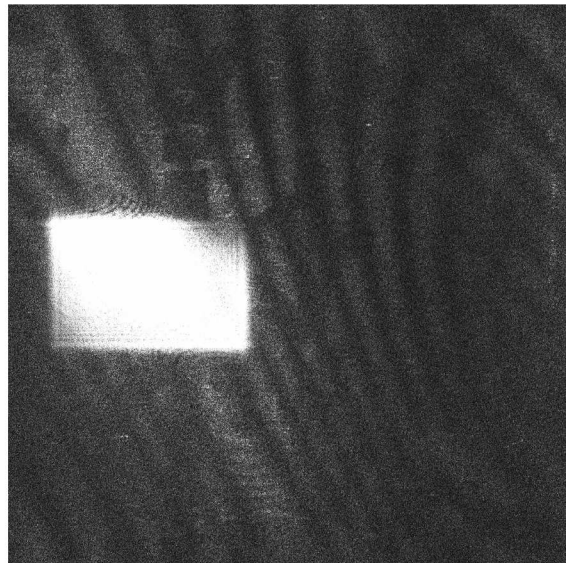
In this chapter, a complete hybrid opto-acoustic vibration analysis system is demonstrated step by step. To do so, first holographic deflection measurement tech-



(a)



(b)



(c)

Figure 5.13: Vibration characteristic of a 2 mm thick aluminum plate. The imaged area is $(3.87\text{ cm} \times 3.87\text{ cm})$ as explained in the text. There are slanted vertical fringes and again the pattern becomes steeper as the voltage is increased from (b) 15V to (c) 30V.

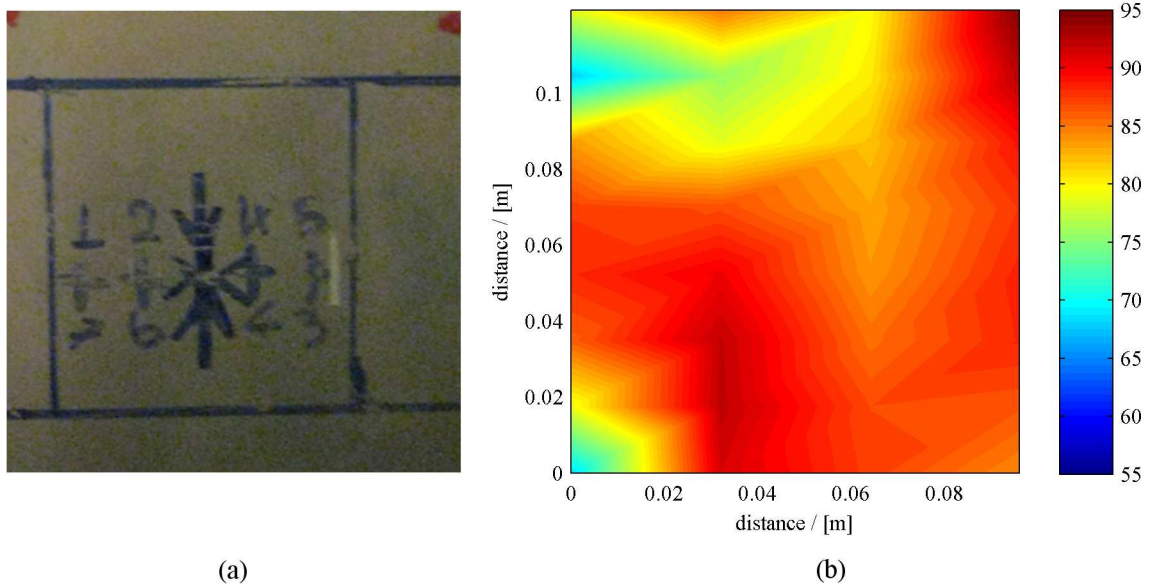


Figure 5.14: Analysis of the aluminum plate using the acoustic system. The imaged area is $(11.2\text{ cm} \times 9.6\text{ cm})$.

nique is explained and its simulations with the PLM method -proposed for the first time in this thesis- is done. Then vibration analysis using holographic interferometry is explained and its simulations again with the PLM are done. Later the microphone array concept which is commonly used in vibration analysis is introduced and experimental results are presented. With this explanation, all of the necessary parts are completed and a hybrid analysis system is constructed by combining the holographic interferometer and the acoustic microphone array. With this system same objects are successfully analyzed both holographically and acoustically. Visually there is a high correlation between the holographic results and the acoustic results.

6 CONCLUSIONS AND FUTURE PROSPECTS

6.1 Conclusion

In this thesis, digital holography is explored both from theoretical and practical aspects. In the theoretical part, a discrepancy in the digital hologram reconstruction that is commonly encountered in the literature is made clear. Then a method (Planar Layers Method or shortly PLM) for calculating the diffraction patterns of objects to be used in CGH is proposed. Accuracy and computational speed analyzes concludes that the new method is an approximate but a fast method compared to the methods in the literature. In the practical issues holographic recording is considered in which two waves namely object wave and the reference wave is required. In the thesis a method to record holograms without a separate reference wave is presented. In the method reference wave is generated from reflecting object wave. In the application side of the holography, holographic deflection measurement and vibration analysis is studied. In this part, a hybrid opto-acoustic imaging system for vibration analysis is successfully demonstrated. As the name implies, the system consist not only of holographic part but also of microphone array. The system is established step by step, first introducing the holographic vibration analysis and then acoustic vibration analysis. In the holographic analysis simulations of the vibrating surfaces are done using PLM. In the acoustic analysis noise pressure maps of the objects are generated. For each step experimental setups are designed, implemented and analysis results are calculated. Visually holographic and acoustic analysis results have a high correlation.

6.2 Future Prospects

In the theoretical part, studied topics are concluded well. In the hybrid opto-acoustic imaging system part, first experiments to prove the concepts are carried out. The experiments are done consecutively, first using the holographic system and then using the acoustic system. As a future work it is possible to integrate these system to work simultaneously. Also, here we studied only the double-exposure time-averaged holographic interferometer in the optical part of the hybrid system to prove our thesis. Different methods such as strobing the reference wave during exposure time or modulating the reference wave to observe larger or smaller vibrations can also be used in the optical part.

Bibliography

- [1] I. Sexton and P. Surman, “Stereoscopic and autostereoscopic display systems,” *IEEE Signal Processing Magazine*, vol. 16, no. 3, pp. 85–99, 1999.
- [2] G. Lippmann, “La photographie integrale,” *Acad. Sci.*, vol. 146, pp. 446–451, 1908.
- [3] D. Gabor, “A new microscopic principle,” *Nature*, vol. 161, pp. 777–778, May 1948.
- [4] T. Okoshi, *Three-dimensional Imaging Techniques*. Academic Press Inc., 1977.
- [5] R. G. Gould, “The laser, light amplification by stimulated emission of radiation,” in *The Ann Arbor Conference on Optical Pumping*, P. Franken and R. Sands, Eds., 1959, p. 128.
- [6] E. N. Leith and J. Upatnieks, “Reconstructed wavefronts and communication theory,” *Journal of the Optical Society of America*, vol. 52, no. 10, pp. 1123–1128, 1962.
- [7] Y. N. Denisyuk, “Photographic reconstruction of the optical properties of an object in its own scattered radiation field,” *Soviet Physics Doklady*, vol. 7, p. 543, 1962.
- [8] R. L. Powell and K. A. Stetson, “Interferometric vibration analysis by wavefront reconstruction,” *Journal of the Optical Society of America*, vol. 55, no. 12, pp. 1593–1598, 1965.
- [9] A. Macovski, “Time-lapse interferometry and contouring using television systems,” *Applied Optics*, vol. 10, no. 12, pp. 2722–2727, 1971.

- [10] J. N. Butters and J. A. Leendertz, “Speckle pattern and holographic techniques in engineering metrology,” *Optics and Laser Technology*, vol. 3, pp. 26–30, 1971.
- [11] B. R. Brown and A. W. Lohmann, “Computer-generated binary holograms,” *IBM Journal of Research and Development*, vol. 13, pp. 160–168, 1969.
- [12] T. S. Huang, “Digital holography,” *Proceedings of the IEEE*, vol. 59, no. 9, pp. 1335–1346, 1971.
- [13] M. A. Kronrod, N. S. Merzlyakov, and L. P. Yaroslavsky, “Reconstruction of a hologram with a computer,” *Soviet Physics-Technical Physics*, vol. 17, no. 2, pp. 419–420, 1972.
- [14] M. Lucente, “Diffraction-specific fringe computation for electro-holography,” Ph.D. dissertation, Massachusetts Institute of Technology, 1994, chairman-Morgenthaler, Frederic R.
- [15] R. S. Pappu, “Minimum information holograms,” Master of Science in Media Arts and Sciences, Massachusetts Institute of Technology, 1995.
- [16] J. W. Goodman, “An introduction to the principles and applications of holography,” in *Proceedings of the IEEE*, vol. 59, no. 9. IEEE, September 1971, pp. 1292–1304.
- [17] Y. Frauel, T. Naughton, O. Matoba, E. Tajahuerce, and B. Javidi, “An introduction to the principles and applications of holography,” in *Three-dimensional Imaging and Processing Using Computational Holographic Imaging*, vol. 94, no. 3. IEEE, March 2006, pp. 636–653.
- [18] Y. Takaki and H. Ohzu, “Hybrid holographic microscopy: visualization of three-dimensional object information by use of viewing angles,” *Applied Optics*, vol. 39, no. 29, pp. 5302–5308, 2000.

- [19] I. Yamaguchi, J. Kato, S. Ohta, and J. Mizuno, “Image formation in phase-shifting digital holography and applications to microscopy,” *Applied Optics*, vol. 40, no. 34, pp. 6177–6186, 2001.
- [20] E. N. Leith and J. Upatnieks, “Holographic imagery through diffusing media,” *Journal of Optical Society of America*, vol. 56, no. 4, pp. 523–523, 1966.
- [21] A. Yariv, “Phase conjugate optics and real-time holography,” *Quantum Electronics, IEEE Journal of*, vol. 14, no. 9, pp. 650–660, Sep 1978.
- [22] Z. Yaqoob, D. Psaltis, M. S. Feld, and C. Yang, “Optical phase conjugation for turbidity suppression in biological samples,” *Nature Photonics*, vol. 2, pp. 110–115, February 2008.
- [23] R. Dändliker and K. Weiss, “Reconstruction of the three-dimensional refractive index from scattered waves,” *Optics Communications*, vol. 1, pp. 323–328, 1970.
- [24] H. Coufal, G. Sincerbox, and D. Psaltis, *Holographic data storage*. Springer-Verlag New York, Inc. Secaucus, NJ, USA, 2000.
- [25] L. Hesselink, S. S. Orlov, and M. C. Bashaw, “Holographic data storage systems,” *Proceedings of the IEEE*, vol. 92, no. 8, August 2004.
- [26] Y. Frauel, E. Tajahuerce, M.-A. Castro, and B. Javidi, “Distortion-tolerant three-dimensional object recognition with digital holography,” *Applied Optics*, vol. 40, no. 23, pp. 3887–3893, 2001.
- [27] T. J. Naughton, Y. Frauel, B. Javidi, and E. Tajahuerce, “Compression of digital holograms for three-dimensional object reconstruction and recognition,” *Applied Optics*, vol. 41, no. 20, pp. 4124–4132, 2002.

- [28] A. Nelleri, U. Gopinathan, J. Joseph, and K. Singh, “Three-dimensional object recognition from digital fresnel hologram by wavelet matched filtering,” *Optics Communications*, vol. 259, pp. 499–506, 2006.
- [29] C. B.-Lefebvre, S. Coëtmellec, D. Lebrun, and C. Özkul, “Application of wavelet transform to hologram analysis: three-dimensional location of particles,” *Optics and Lasers in Engineering*, vol. 33, pp. 409–421, 2000.
- [30] Y. Aoki, “Watermarking technique using computer-generated holograms,” *Electronics and Communications in Japan, Part 3*, vol. 84, no. 1, pp. 21–31, 2001.
- [31] L. Onural, A. Gotchev, H. M. Özaktaş, and E. Stoykova, “A survey of signal processing problems and tools in holographic three-dimensional television,” *IEEE Transaction on Circuits and Systems for Video Technology*, vol. 17, no. 11, pp. 1631–1646, 2007.
- [32] J. C. Dainty, “Laser speckle and related phenomena,” *Topics in Applied Physics*, vol. 9, 1975.
- [33] U. Schnars and W. Jüptner, “Direct recording of holograms by a CCD target and numerical reconstruction,” *Applied Optics*, vol. 33, no. 2, pp. 179–181, 1994.
- [34] M. Özcan and M. Bayraktar, “Digital holography image reconstruction methods,” vol. 7233, no. 1. SPIE, 2009, p. 72330B.
- [35] M. Bayraktar and M. Özcan, “A new method for computer generated holography of 3D objects,” *ISCIS 2009*, Sept. 2009, pp. 66–69.
- [36] M. Özcan and M. Bayraktar, “Holographic recording without a separate reference wave.” SPIE, 2010.

- [37] J. W. Goodman, *Introduction to Fourier Optics*, 2nd ed. New York: McGraw-Hill Companies, Inc., 1996.
- [38] Y. Takaki, H. Kawai, and H. Ohzu, “Hybrid holographic microscopy free of conjugate and zero-order images,” *Applied Optics*, vol. 38, no. 23, pp. 4990–4996, 1999.
- [39] Y. Awatsuji, M. Sasada, and T. Kubota, “Parallel quasi-phase-shifting digital holography,” *Applied Physics Letters*, vol. 85, no. 6, pp. 1069–1071, 2004.
- [40] Y. Awatsuji, M. Sasada, A. Fujii, and T. Kubota, “Scheme to improve the reconstructed image in parallel quasi-phase-shifting digital holography,” *Applied Optics*, vol. 45, no. 5, pp. 968–974, 2006.
- [41] Y. Awatsuji, A. Fujii, T. Kubota, and O. Matoba, “Parallel three-step phase-shifting digital holography,” *Applied Optics*, vol. 45, no. 13, pp. 2995–3002, 2006.
- [42] T. Nomura, S. Murata, E. Nitani, and T. Numata, “Phase-shifting digital holography with a phase difference between orthogonal polarizations,” *Applied Optics*, vol. 45, no. 20, pp. 4873–4877, 2006.
- [43] Y. Awatsuji, T. Tahara, A. Kaneko, T. Koyama, K. Nishio, S. Ura, T. Kubota, and O. Matoba, “Parallel two-step phase-shifting digital holography,” *Applied Optics*, vol. 47, no. 19, pp. D183–D189, 2008.
- [44] E. CuChe, P. Marquet, and C. Depeursinge, “Spatial filtering for zero-order and twin-image elimination in digital off-axis holography,” *Applied Optics*, vol. 39, no. 23, pp. 4070–4075, 2000.
- [45] G. Pedrini, S. Schedin, and H. J. Tiziani, “Spatial filtering in digital holographic microscopy,” *Journal of Modern Optics*, vol. 47, pp. 1447–1454(8), 10 July 2000.

- [46] Y. Zhang, Q. Lü, and B. Ge, “Elimination of zero-order diffraction in digital off-axis holography,” *Optics Communications*, vol. 240, no. 4-6, pp. 261 – 267, 2004.
- [47] M. Liebling, T. Blu, and M. Unser, “Fresnelets: New multiresolution wavelet bases for digital holography,” *IEEE Transactions on Image Processing*, vol. 12, no. 1, pp. 29–43, 2003.
- [48] M. Liebling, T. Blu, and M. A. Unser, “Non-linear fresnelet approximation for interference term suppression in digital holography,” M. A. Unser, A. Aldroubi, and A. F. Laine, Eds., vol. 5207, no. 1. SPIE, 2003, pp. 553–559.
- [49] L. Onural and P. Scott, “Digital decoding of in-line-holograms,” *Optical Engineering (Bellingham. Print)*, vol. 26, no. 11, pp. 1124–1132, 1987.
- [50] T. Kim, T. Poon, and G. Indebetouw, “Twin-Image Removal by Digital Filtering and Optical Scanning Holography,” in *Southeastern Symposium on System Theory*, vol. 30. IEEE Computer Society Press, 1998, pp. 191–195.
- [51] T. C. Lee, “Holographic recording on thermoplastic films,” *Applied Optics*, vol. 13, no. 4, pp. 888–895, 1974.
- [52] K. Matsushima, “Computer-generated holograms for three-dimensional surface objects with shade and texture,” *Applied Optics*, vol. 44, no. 22, pp. 4607–4614, 2005.
- [53] R. Ziegler, P. Kaufmann, and M. Gross, “A framework for holographic scene representation and image synthesis,” *IEEE Transactions on Visualization and Computer Graphics*, vol. 13, no. 2, pp. 403–415, 2007.

- [54] U. Schnars and W. Juptner, “Digital recording and numerical reconstruction of holograms,” *Measurement Science and Technology*, vol. 13, no. 9, pp. R85–R101, Sept. 2002.
- [55] T. M. Kreis, M. Adams, and W. P. O. Jueptner, “Methods of digital holography: a comparison,” C. Gorecki, Ed., vol. 3098, no. 1. SPIE, 1997, pp. 224–233.
- [56] U. Schnars and W. Jueptner, *Digital Holography: Digital Hologram Recording, Numerical Reconstruction, and Related Techniques*. Springer-Verlag, 2005.
- [57] G. Esmer and L. Onural, “Simulation of scalar optical diffraction between arbitrarily oriented planes,” *1st Int. Symp. on Control, Communications and Signal Processing*, pp. 225–228, 2004.
- [58] F. Shen and A. Wang, “Fast-fourier-transform based numerical integration method for the RayleighSommerfeld diffraction formula,” *Applied Optics*, vol. 45, no. 6, pp. 1102–1110, 2006.
- [59] S. Ganci, “Fourier diffraction through a tilted slit,” *European Journal of Physics*, vol. 2, pp. 158–160, 1981.
- [60] K. Patorski, “Fraunhofer diffraction patterns of titled planar objects,” *Journal of Modern Optics*, vol. 30, pp. 673–679(7), May 1983.
- [61] H. J. Rabal, N. Bolognini, and E. E. Sicre, “Diffraction by a tilted aperture,” *Journal of Modern Optics*, vol. 32, pp. 1309–1311(3), November 1985.
- [62] D. Leseberg and C. Frère, “Computer-generated holograms of 3-D objects composed of tilted planar segments,” *Applied Optics*, vol. 27, no. 14, pp. 3020–3024, 1988.

- [63] C. Frère and D. Leseberg, “Large objects reconstructed from computer-generated holograms,” *Applied Optics*, vol. 28, no. 12, pp. 2422–2425, 1989.
- [64] T. Tommasi and B. Bianco, “Frequency analysis of light diffraction between rotated planes,” *Optics Letters*, vol. 17, no. 8, pp. 556–558, 1992.
- [65] T. Tommasi and B. Bianco, “Computer-generated holograms of tilted planes by a spatial frequency approach,” *Journal of Optical Society of America A*, vol. 10, no. 2, pp. 299–305, 1993.
- [66] B. Bianco and T. Tommasi, “Space-variant optical interconnection through the use of computer-generated holograms,” *Applied Optics*, vol. 34, no. 32, pp. 7573–7580, 1995.
- [67] N. Delen and B. Hooker, “Free-space beam propagation between arbitrarily oriented planes based on full diffraction theory: A fast fourier transform approach,” *Journal of Optical Society of America A*, vol. 15, pp. 857–867, 1998.
- [68] K. Matsushima, H. Schimmel, and F. Wyrowski, “Fast calculation method for optical diffraction on tilted planes by use of the angular spectrum of plane waves,” *Journal of Optical Society of America A*, vol. 20, no. 9, pp. 1755–1762, 2003.
- [69] D. Mas, J. Garcia, C. Ferreira, L. M. Bernardo, and F. Marinho, “Fast algorithms for free-space diffraction patterns calculation,” *Optics Communications*, vol. 164, pp. 233–245, 1999.
- [70] H. M. Ozaktas, A. Koc, I. Sari, and M. A. Kutay, “Efficient computation of quadratic-phase integrals in optics,” *Optics Letters*, vol. 31, pp. 35–37, 2006.
- [71] L. Onural, “Diffraction from a wavelet point of view,” *Optics Letters*, vol. 18, pp. 846–848, 1993.

- [72] L. Onural and M. Kocatepe, “Family of scaling chirp functions and diffraction and holography,” *IEEE Transactions on Signal Processing*, vol. 43, no. 7, pp. 1568–1578, July 1995.
- [73] D. Leseberg, “Computer generated holograms: cylindrical, conical, and helical waves,” *Applied Optics*, vol. 26, no. 20, pp. 4385–4390, 1987.
- [74] J. Rosen, “Computer-generated holograms of images reconstructed on curved surfaces,” *Applied Optics*, vol. 38, no. 29, pp. 6136–6140, 1999.
- [75] N. M. Spornik and A. F. Tujev, “Universal interferometer with synthesized reference wave,” in *Proceedings of the SPIE*, vol. 1508. SPIE, 1991, pp. 83–88.
- [76] V. V. Aristov, V. G. Lysenko, V. B. Timofeev, and V. S. Shekhtman, “Holography without a reference beam for three-dimensional holograms,” *Soviet Physics–Dokl*, vol. 13, no. 12, pp. 1222–1224, 1969.
- [77] H. J. Caulfield, J. G. Cobb, J. L. Harris, H. W. Hemstreet, and J. R., “Local reference beam generation in holography,” in *Proceedings of IEEE*, vol. 55, no. 10. IEEE, October 1967, pp. 1758 –1758.
- [78] L. Rosen and W. Clark, “Film plane holograms without external source reference beams,” *Applied Physics Letters*, vol. 10, no. 5, pp. 140–142, 1967.
- [79] O. J. Løkberg, “Use of chopped laser light in electronic speckle pattern interferometry,” *Applied Optics*, vol. 18, no. 14, pp. 2377–2384, 1979.
- [80] G. Å. Slettemoen, “Electronic speckle pattern interferometry system based on a speckle reference beam,” *Applied Optics*, vol. 19, no. 4, pp. 616–623, 1980.
- [81] S. Nakadate, T. Yatagai, and H. Saito, “Digital speckle-pattern shearing interferometry,” *Applied Optics*, vol. 19, no. 24, pp. 4241–4246, 1980.

- [82] O. J. Løkberg and G. Å. Slettemoen, “Interferometric comparison of displacements by electronic speckle pattern interferometry,” *Applied Optics*, vol. 20, no. 15, pp. 2630–2634, 1981.
- [83] O. J. Løkberg, “ESPI—the ultimate holographic tool for vibration analysis?” *Journal of Acoustical Society of America*, vol. 75, no. 6, pp. 1783–1791, 1984.
- [84] G. Pedrini and H. J. Tiziani, “Double-pulse electronic speckle interferometry for vibration analysis,” *Applied Optics*, vol. 33, no. 34, pp. 7857–7863, 1994.
- [85] K. Høgmoen and O. Løkberg, “Detection and measurement of small vibrations using electronic speckle pattern interferometry,” *Applied Optics*, vol. 16, no. 7, pp. 1869–1875, 1977.
- [86] M. Brandstein and D. Ward, *Microphone arrays: signal processing techniques and applications*. Birkhäuser, 2001.
- [87] J. Benesty, J. Chen, and Y. Huang, *Microphone Array Signal Processing*, J. Benesty and W. Kellerman, Eds. Springer-Verlag, 2008.